coatings

MDPI

Article

Study on Eccentric Compression Mechanical Characteristics of Basalt Fiber-Reinforced Recycled Aggregate Concrete-Filled Circular Steel Tubular Column

Xianggang Zhang [1,2], Jixiang Niu [2], Shuai Qiao [3], Chengyi Luo [2], Yuhui Fan [2,*], Xiaomei Kuang [2] and Yajun Huang [1]

[1] School of Intelligent Construction, Wuchang University of Technology, Wuhan 430223, China; xgzhang1986@163.com (X.Z.); hyjwut@163.com (Y.H.)
[2] School of Civil Engineering, Henan Polytechnic University, Jiaozuo 454003, China; njx13137175511@163.com (J.N.); luochengyi1999@163.com (C.L.); kuangxm123@126.com (X.K.)
[3] Changzheng Engineering Co., Ltd., Beijing 101111, China; qiaoshuai@china-ceco.com
* Correspondence: fyhlgd@126.com

Abstract: During this study, eight basalt fiber-reinforced recycled aggregate concrete-filled circular steel-tubular (C-BFRRACFST) column specimens were subjected to eccentric compression tests with different replacement ratios of recycled coarse aggregate (RCA), basalt fiber (BF) contents, length-diameter (L/D), and eccentricity. The whole process of stress as well as failure mode of the specimens were observed, and a load–displacement curve as well as a load–strain curve for the specimens were measured. The impacts of various parameters upon the bearing capacity, peak displacement, and ductility coefficient of the specimens were analyzed. Subsequently, a 3D finite element model of the C-BFRRACFST column was established, and the whole process of stress was simulated. Based on the finite element simulation results, the N/N_u-M/M_u correlation strength curve of the C-BFRRACFST columns was verified. The exploration demonstrated that under eccentric load, the C-BFRRACFST column eventually underwent destruction of the overall instability. The load–axial displacement curve was characterized as three stress stages: elastic, elastic–plastic, declining, as well as declining stages. The strain of the mid-span section for the specimens follows the plane section assumption, and the lateral deflection basically follows the sine waveform curve. The ultimate bearing capacity of the specimens exhibited little change as the replacement ratio of RCA improved, while the ductility progressively reduced. Furthermore, the ultimate bearing capacity of the specimens failed to be obviously changed as the BF content enhanced, while the ductility progressively rose. Increasing the L/D gradually reduced the specimen's ultimate bearing capacity alongside its ductility. The corrected N/N_u-M/M_u curve agreed well with the findings of finite element simulation.

Keywords: recycled aggregate concrete-filled circular steel tubular; basalt fiber; eccentric compression; finite element analysis; ductility; *N/Nu-M/Mu* correlation strength curve

Citation: Zhang, X.; Niu, J.; Qiao, S.; Luo, C.; Fan, Y.; Kuang, X.; Huang, Y. Study on Eccentric Compression Mechanical Characteristics of Basalt Fiber-Reinforced Recycled Aggregate Concrete-Filled Circular Steel Tubular Column. *Coatings* **2023**, *13*, 1923. https://doi.org/10.3390/coatings13111923

Academic Editor: Andrea Nobili

Received: 3 October 2023
Revised: 31 October 2023
Accepted: 6 November 2023
Published: 10 November 2023

1. Introduction

Construction waste is growing and material resources are becoming scarcer as urbanization progresses. Construction waste is currently treated in an inefficient method that wastes an enormous number of resources. Among them, waste concrete accounts for a significant amount of construction waste. Therefore, the solution to the inappropriate handling of construction waste as well as the lack of material resources is to figure out how to efficiently treat and utilize waste concrete. This process is known as "turning waste into treasure" [1–3]. Soon afterwards, recycled aggregate concrete (RAC) technology emerged. The RAC technology uses RCA formed by waste concrete to replace natural coarse aggregate (NCA) to configure concrete, which can not only reduce the consumption of NCA in construction industry, but also solves the problem of secondary pollution caused by the stacking, occupation, and improper treatment of waste concrete. This complies with

environmental and resource sustainability standards [4,5]. Therefore, this technology has received extensive attention from researchers. Research has revealed that RCA manufacturing results in micro-cracks, which diminish the strength and elastic modulus of RCA compared to concrete [6–8].

Researchers have conducted an abundance of research to enhance RAC's performance [9–11]. The desired improvement in RAC's mechanical characteristics failed to be achieved by altering the mix ratio of RAC as well as the treatment of RCA. Therefore, researchers have proposed an RAC-filled steel tube (RACFST) along with fiber-reinforced RAC [12–14]. The former uses steel tubes to constrain the lateral deformation of RAC, thereby improving the RAC's mechanical characteristics. The latter uses fiber to improve the mechanical properties of RAC. Numerous investigations of these two structures are currently being conducted.

In the area of RACFST, Liu et al. [15] examined the constraining impact of steel tubes on RAC in RACFST columns. The findings demonstrate that the steel tube constraint improves the mechanical characteristics of RAC, and the performance of RACFST columns was comparable to that of concrete filled steel tube columns (CFST). Yang et al. [16] conducted research on RACFST members' performance. The outcome revealed that under identical loading circumstances, RACFST members had qualities similar to CFST members, but the stiffness as well as bearing capacity were less than those of CFST members. Chen et al. [17] conducted experimental research to investigate the seismic performance of RACFST columns. The results illustrate that square RACFSTs perform well in seismic tests. According to the findings, square RACFSTs performed well during earthquakes. The seismic performance for RACFST members was investigated by Huang et al. [18]. The findings demonstrate that the RACFST members' seismic performance was dependent on RAC content, as well as the damage index, which improved as the replacement ratios enhanced. The research on the RACFST columns' bearing capacity was carried out by Liu et al. [19]. The conclusions demonstrate that the addition of RAC would not cause a reduction in the column's lateral stiffness, and that RACFST columns possess a similar energy dissipation capacity as CFST columns. The application of RAC exerts little impact upon the lateral bearing capacity nor the stiffness degradation of RACFST columns. Jin et al. [20] carried out finite element analysis on RACFST columns' bearing capacity. The results demonstrated that RAC members' mechanical characteristics as well as deformation behavior were similar to those of ordinary concrete members.

In terms of fiber-reinforced RAC, Dong [21], Zheng [22], and Liu [23] studied the mechanical characteristics as well as microstructure of basalt fiber-reinforced recycled aggregate concrete (BFRRAC). The findings show that the addition of BF can not only enhance RAC, but also improve the microstructure of the interfacial transition zone, thus further enhancing RAC's strength as well as ductility. Li et al. [24] investigated the flexural performance of unbonded prestressed BFRRAC beams. The outcomes proved that the incorporation of BF into RAC can effectively enhance mortar adhesion on the surface of RCA, inhibit crack development, as well as enhance ductility. Huang et al. [25] researched the mechanical characteristics of BFRRAC. As a consequence, the flexural strength and splitting tensile strength of RAC were considerably increased after incorporating BF, whereas the compressive strength initially increased and then subsequently decreased as the fiber content increased. The effect of BF upon RAC performance was examined by Du et al. [26]. The findings reveal that incorporating BF can enhance RAC's mechanical characteristics as well as durability. Katkhuda et al. [27] investigated the impact on the mechanical characteristics of RAC with chopped BF as well as acid treatment. According to their findings, incorporating chopped basalt fiber into RAC shows little impact on compressive strength, while it considerably improves the flexural as well as splitting tensile strengths. The quality and mechanical characteristics of RAC were considerably improved by the application of low concentration acid. Shatarat et al. [28] explored the impact of BF on the bond strength of RAC. The outcomes indicated that the RAC's bond strength increased as the BF content increased. In summary, fiber-reinforced RAC as well as RACFST both had the ability to

significantly enhance the quality and mechanical characteristics of RAC, bringing it closer to concrete's performance. Therefore, RACFST and fiber-reinforced RAC could replace ordinary concrete for practical engineering.

With the development in research, researchers have discovered that the combination of the RACFST structure and the fiber-reinforced RAC structure form a fiber-reinforced RACFST composite structure, which can not only combine the advantages of the RACFST structure and the fiber-reinforced RAC, but also further enhance the utilization of construction waste. BF is an inorganic fiber material that possesses high strength, durability, chemical stability, as well as environmental friendliness. Proper BF content can considerably enhance the performance of RAC [29,30]. Currently, there are few studies on basalt fiber-reinforced recycled aggregate concrete-filled circular steel tubes (BFRRACFSTs). This work investigates the eccentric compression mechanical characteristics of C-BFRRACFST columns through existing research. Eight C-BFRRACFST column specimens were constructed for this investigation, and eccentric compression tests were performed to investigate the specimens' failure mode and examine their eccentric compression performance. This provides a reference for further research on BFRRACFST's structure.

2. Experimental Overviews

2.1. Design and Manufacture of Specimens

In this study, the core RAC was manufactured by utilizing P·O42.5 grade cement, natural yellow sand, urban tap water, grade II fly ash, high-performance water reduction agent, natural coarse aggregate (NCA), as well as RCA. The mix ratio of RAC under various replacement ratios is illustrated in Table 1. In addition, this study employed chopped BF, of which the outer diameter, length, and density were 15 μm, 18 mm, and 2650 kg/m^3, respectively. In addition, its tensile strength was 4500 MPa, elastic modulus was 104 GPa, and elongation at break was 3.1%. According to "Standard for Test Methods of Physical and Mechanical Properties of Concrete" (China GB/T 50081-2019 [31]), the performance indexes of basalt fiber-reinforced recycled aggregate concrete (BFRRAC) were measured, which is illustrated in Table 2. The test was carried out using seamless steel tubes of Q235 grade with an outer diameter of 114 mm and a thickness of 3.5 mm. According to "Metallic Materials Tensile Testing Part 1: Method of Test at Room Temperature" (China GB/T 228.1-2021 [32]), the measured yield strength and ultimate strength of steel tube were 318.76 MPa and 373.27 MPa, respectively, while the yield strain was 1758 με, elastic modulus was 181 GPa, and Poisson's ratio was 0.33.

Table 1. Mix ratios of RAC (kg/m^3).

r/%	Water–Binder Ratio	Sand Ratio/%	Water		Cementitious Materials		Coarse Aggregate		Sand	Water-Reducing Agent
			Net Water	Additional Water	Cement	Fly Ash	RCA	NCA		
0	0.40	31	205	0.0	427.1	85.4	0.0	1115.2	501	2.56
50	0.40	31	205	31.2	427.1	85.4	557.6	557.6	501	2.56
100	0.40	31	205	62.5	427.1	85.4	1115.2	0.0	501	2.56

Note: Recycled coarse aggregate was obtained by manual crushing, grading screening, as well as drying of reinforced-concrete beams with an original concrete design strength grade of C25. Additional water was then needed after considering the water absorption of RCA. The fineness of grade II fly ash was 43 μm, the density was 2.34 g/cm^3, and the dosage was 20% of the cement. The amount of water reducer was 0.5% of cementitious materials (cement and fly ash).

Table 2. Performance indexes of BFRRAC.

r (%)	m_{BF} (kg/m^3)	f_{cu} (MPa)	f_c (MPa)	E_c (GPa)	ν_c
0	2	52.8	41.5	33.5	0.22
	0	48.5	34.9	29.2	0.23
50	2	50.7	36.1	31.4	0.20
	4	51.9	38.5	34.6	0.18
100	2	46.1	32.2	28.3	0.19

Note: m_{BF} represents BF content; f_{cu} represents the cube compressive strength value; f_c represents the compressive strength of prism; E_c represents the elastic modulus, followed by its value was the ratio of the stress at $0.5f_c$ on the BFRRAC stress–strain curve to the corresponding strain; ν_c represents Poisson's ratio.

During this study, eight C-BFRRACFST column specimens were subjected to eccentric compression tests with various replacement ratios of RCA (0%, 50%, 100%), BF contents (0, 2, 4 kg/m^3), L/D (5, 8, 11), along with eccentricity (35 mm, 70 mm). When making the specimen, a 150 mm × 150 mm × 10 mm cover plate was first aligned with the geometric center of one end of the steel tube and then welded to seal the bottom. After that, well-mixed concrete was poured from the top, and was continuously vibrated with a vibrating rod until the concrete was dense. After standing at room temperature for 24 h, and when the shrinkage deformation of concrete failed to be obvious, cement mortar of the same strength grade was prepared to smooth the shrinkage gap. After 7 days, the other end of the steel tube was capped with the same cover plate and cured at room temperature. The relevant parameters and measured values for each specimen are shown in Table 3.

Table 3. Related parameters and measured strength of specimens under eccentric compression.

Specimen Number	L (mm)	L/D	e	α	ξ	N_u (kN)	Peak Displacement (mm)
CE-0-2-8-35	912	8	35	0.1351	1.038	566.04	6.2
CE-100-2-8-35	912	8	35	0.1351	1.338	567.07	7.47
CE-50-2-8-35	912	8	35	0.1351	1.193	566.22	6.71
CE-50-2-8-70	912	8	70	0.1351	1.193	416.29	8.22
CE-50-0-8-35	912	8	35	0.1351	1.234	568.01	8.51
CE-50-4-8-35	912	8	35	0.1351	1.119	561.85	6.07
CE-50-2-5-35	570	5	35	0.1351	1.193	659.33	8.55
CE-50-2-11-35	1254	11	35	0.1351	1.193	512.59	8.68

Note: α represents the steel ratio, $\alpha = A_s/A_c$, A_s, A_c represent the cross-sectional area of steel tube and core concrete, respectively; ξ represents the constraint effect coefficient, $\xi = \alpha f_y/f_c$; N_u represents the specimen's peak load; the naming method for specimen takes CE-50-2-8-35 as an example. CE represents the eccentrically compressed specimen, 50 represents the replacement ratio of RCA, 2 represents BF content, 8 represents length-diameter ratio, and 35 represents eccentricity.

2.2. Test Device

The image of the loading device is depicted in Figure 1a, the schematic of the loading is depicted in Figure 1b, and the cross section of specimen 1-1 is depicted in Figure 1c. The test adopted the loading method of force and displacement combined control. Preloading was performed before formal loading, held for 2 min, and then unloaded. At the beginning of loading, the load was graded according to the $P_u/10$ of its ultimate load, and each load was loaded for 2 min until it reached 0.90 P_u. Subsequently, the force control was converted to displacement control, and the displacement difference was about 1 mm. Once the load dropped to 70% of the ultimate load, the test was completed.

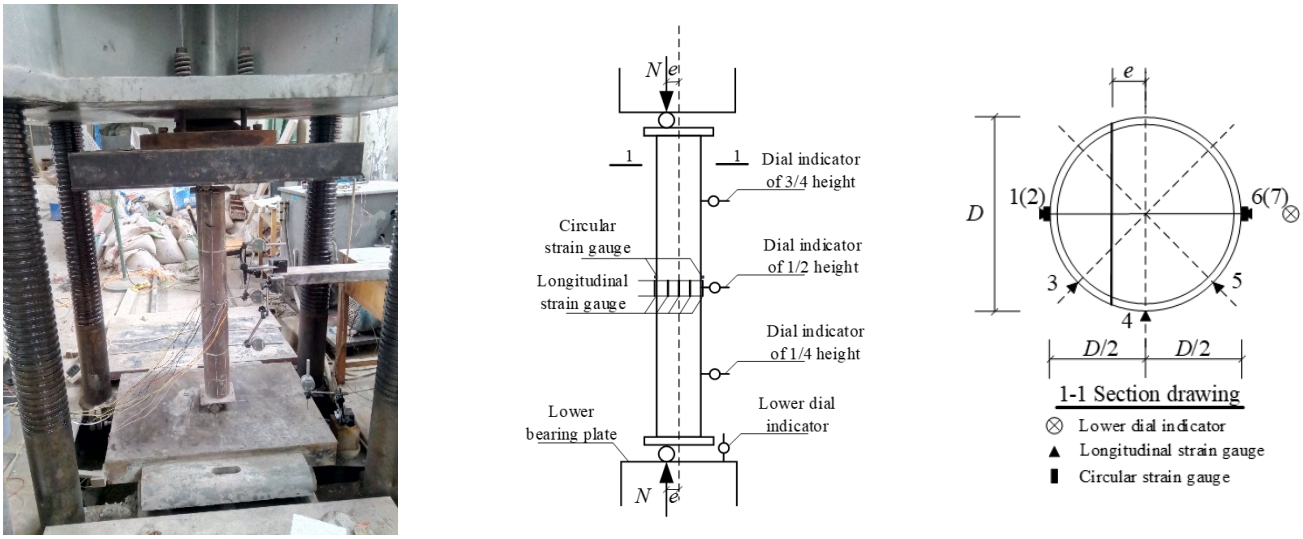

(**a**) Image of loading device (**b**) Schematic of the loading (**c**) Specimen 1-1 section

Figure 1. Loading device of the specimen.

3. Experiment Results and Analyses

3.1. Failure Mode and Load–Lateral Displacement Curve

Three displacement meters (represented by a, b, and c, respectively) were arranged at 3/4, 1/2, and 1/4 heights of the tensile side of the specimens to measure their lateral deflection value (δ) at different heights under eccentric compression load (N). The failure modes and load-up/mid/down displacement curves for each specimen are shown in Figure 2.

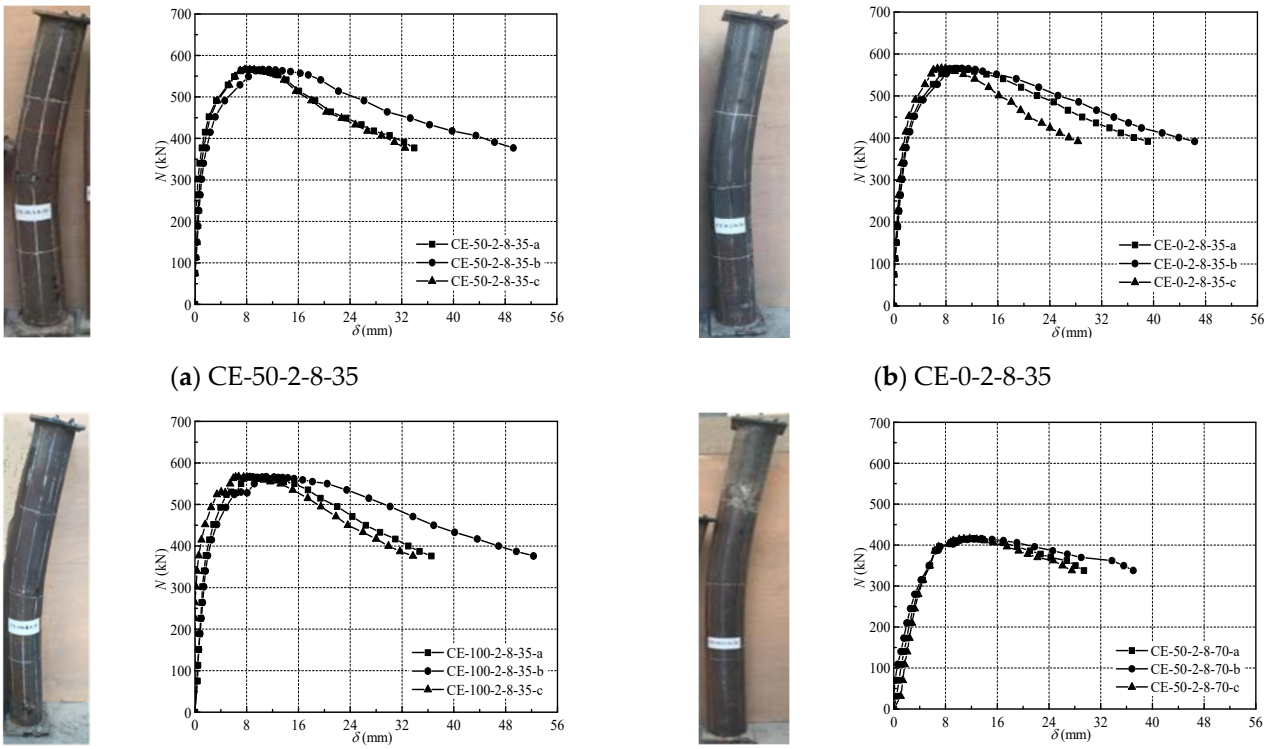

(**a**) CE-50-2-8-35 (**b**) CE-0-2-8-35

(**c**) CE-100-2-8-35 (**d**) CE-50-2-8-70

Figure 2. *Cont.*

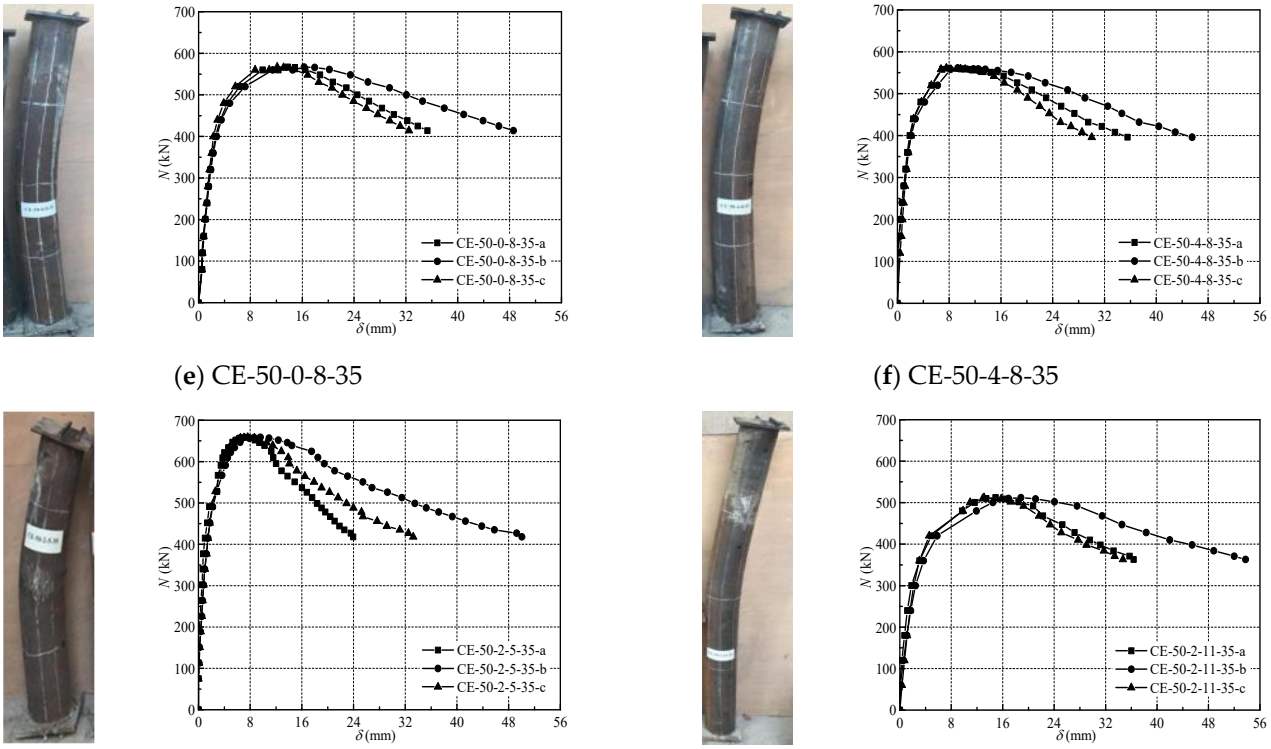

(**e**) CE-50-0-8-35 (**f**) CE-50-4-8-35

(**g**) CE-50-2-5-35 (**h**) CE-50-2-11-35

Figure 2. The failure mode and load-up/mid/down displacement curves for each specimen.

As displayed in Figure 2, the load–lateral displacement curve of the specimens can be separated into three stages: elastic, elastoplastic, and descending. The specimens' load–lateral displacement curve is in the elastic stage at the initial stage of loading, and the curve develops linearly. As the load continually grows, and under the action of and additional bending moment, the lateral expansion deformation of the core BFRAC in the tension and compression zone, as well as the steel tube's constraint effect upon the core BFRAC, interact with each other. As the steel tube approaches yield value, the stiffness decreases, and the specimens produce a slight lateral deflection. The specimens' load–lateral displacement curve subsequently enters the elastic–plastic phase. After reaching the peak load, the load–lateral displacement curves for the specimens enter the descending section, and the load begins to decline slowly. As the load continues to be loaded, the specimens' capacity to resist bending moment deformation cannot keep up with the speed of deflection deformation, and the additional bending moment is further increased. The bearing capacity begins to decrease at a faster rate, and the deflection of the specimens further develops. Finally, severe plastic deformation develops locally in the middle of the specimens, and the test is terminated.

Following the test, specimen CE-50-2-8′s outer steel tube was cut apart to reveal the core BFRRAC's failure mode, which is illustrated via Figure 3a. The failure modes of the core BFRRAC along with different heights and directions were observed. An actual diagram of the internal BFRAC crack is described in Figure 3b, and the schematic diagram of the internal BFRAC crack is described by Figure 3c. Firstly, as can be clearly identified in Figure 3b ①, there are only a few transverse cracks and gaps in the specimen's upper tensile zone. In addition, there are no cracks close to the gaps, and the lower-part cracks are denser. Secondly, as illustrated in Figure 3b ②, the fully developed and dense transverse cracks along the height of the specimen can be clearly observed in the tensile zone with the largest deflection. Despite being severely damaged throughout, the concrete can nonetheless retain its current condition of cracking and not disperse. Thirdly, according to Figure 3b ③, when the specimen is damaged, the BFRRAC in the compressive zone is obviously fractured,

and a certain number of oblique cracks and small longitudinal cracks are distributed in the fractured zone. Fourth, as illustrated in Figure 3b ④, a wide transverse crack crosses the core BFRRAC's tensile and compressive zone, and there is a large gap in the transverse crack. This can be explained as the concrete in this area is partially crushed, and the crushed local cement mortar is firmly bonded to the steel tube, so the local concrete adheres to the stripped steel tube to form a larger gap. Fifth, from Figure 3b ⑤, the transverse cracks in the lower tensile zone of the specimen are thin and long. Finally, the overall shape of core BFRRAC is relatively complete. It can be seen that the concrete has good contact with steel tube after forming, and there is no considerable honeycomb surface phenomenon.

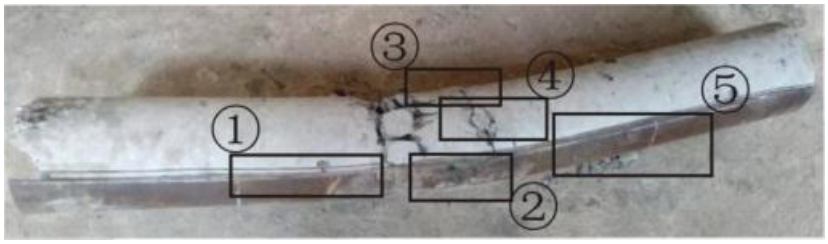

(**a**) The overall failure mode of the specimen

(**b**) Internal BFRAC

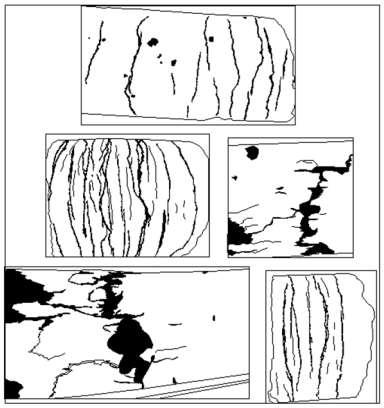

(**c**) Internal BFRAC crack diagram

Figure 3. Failure mode of specimen.

In summary, the test deformation process and macroscopic phenomenon of C-BFRRACFST under eccentric compression are similar. As the load increased, the flexural deformation in the specimen's middle tension increased continuously, the second-order effect was obvious, and the bearing capacity of the specimen seriously decreased. For the specimens with an L/D of 8 and 11, the final failure mode was bending failure caused by the global buckling of the steel tube; for the specimens with an L/D of 5, the final failure mode was bending failure caused by the the interaction between global buckling and local buckling. During the specimens' whole eccentric loading process, the deformation gradually increased, and the C-BFRRACFST column shows good ductility during the loading process.

3.2. Load–Axial Displacement Curve

Figure 4 depicts the load (N)–axial displacement (Δ) relationship curve for the C-BFRRACFST columns subjected to eccentric compression loads with various replacement ratios of RCA, BF contents, L/D, and eccentricity. The curves for each specimen can be separated into three stress stages: elastic, elastic–plastic, and declining stages. The following findings were reached via comparison and analysis.

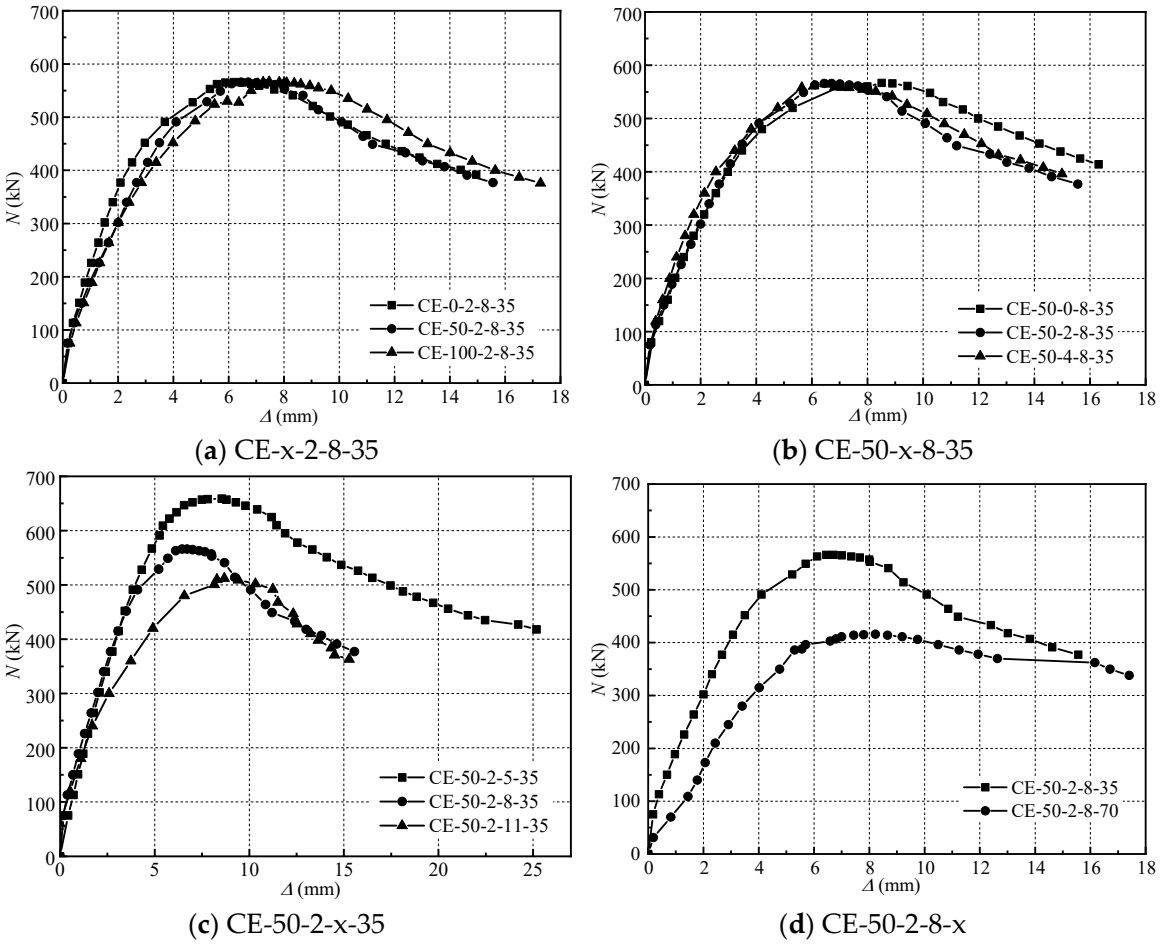

Figure 4. Comparison of load–axial displacement curves.

(1) As shown in Figure 4a, under the BF content, L/D and eccentricity remain unchanged and increasing the replacement ratios of RCA gradually decreased the slope for specimen's load–axial displacement curve during elastic and elastic–plastic stages, indicating a reduction in the specimen's stiffness. After attaining the ultimate bearing capacity, each specimen's curve entered the declining section, and both the curves' development trend and variation range are essentially the same.

(2) As demonstrated in Figure 4b, the specimen's curve exhibits little difference between the elastic and elastic–plastic stages when the replacement ratio of RCA, L/D, and eccentricity are kept constant. As the load approached the ultimate bearing capacity, specimen CE-50-0-8-35′s axial displacement became larger, indicating that the specimen's ductility increased as the BF content increased.

(3) As illustrated from Figure 4c, keeping the BF content the same caused the replacement ratio of RCA and eccentricity to remain unchanged. The slope for the specimen's load–axial displacement curve during the rising section decreased as the L/D improved, that is, the specimen's stiffness gradually decreased. After reaching the ultimate bearing capacity, the declining section of specimen CE-50-2-5-35 was gentle, indicating when L/D was improved, the specimen's bearing capacity in the declining section decreased sharply.

(4) As demonstrated in Figure 4d, under the BF content, the L/D as well as replacement ratio of RCA remain unchanged; furthermore, the larger the eccentricity, the smaller the slope of specimen's load–axial displacement curve. After reaching the ultimate bearing capacity, specimen CE-50-2-8-35′s bearing capacity decreased sharply. At the end of loading, the two specimens' development trend was consistent. It was demonstrated that as the eccentricity increased, the specimen's maximum bearing

capacity slowly reduced, and the bearing capacity reduced slowly after reaching the ultimate bearing capacity.

3.3. Deflection Sine Half-Wave Curve Height–Lateral Deflection Curve

Several specimens' lateral deflection distribution curves along the column height at various loading stages are illustrated in Figure 5. Among them, N_u represents the specimen's peak load, the positive value of 0.90 N_u indicates the load level before the ultimate load, and the negative value of 0.99 N_u indicates the load level after the ultimate load. At the beginning of loading, the specimens' lateral deflection was small, and the lateral deflection distribution curves along the column height were nearly straight. The specimen's midsection experienced the maximum lateral deformation as the load increased, but overall, the specimen's lateral deformation was symmetrical along the middle, indicating that the material distribution inside the specimen was more uniform and the load was more uniform along the specimen's vertical direction. As the load further increased, each specimen's lateral deflection deformation gradually resembled a sinusoidal half-wave curve. The simulated sinusoidal half-wave curve has a high level of compatibility with the lateral deflection distribution curve, indicating that the lateral deflection development of the C-BFRRACFST column under eccentric compression at different stages of loading almost corresponds to the sinusoidal half-wave curve.

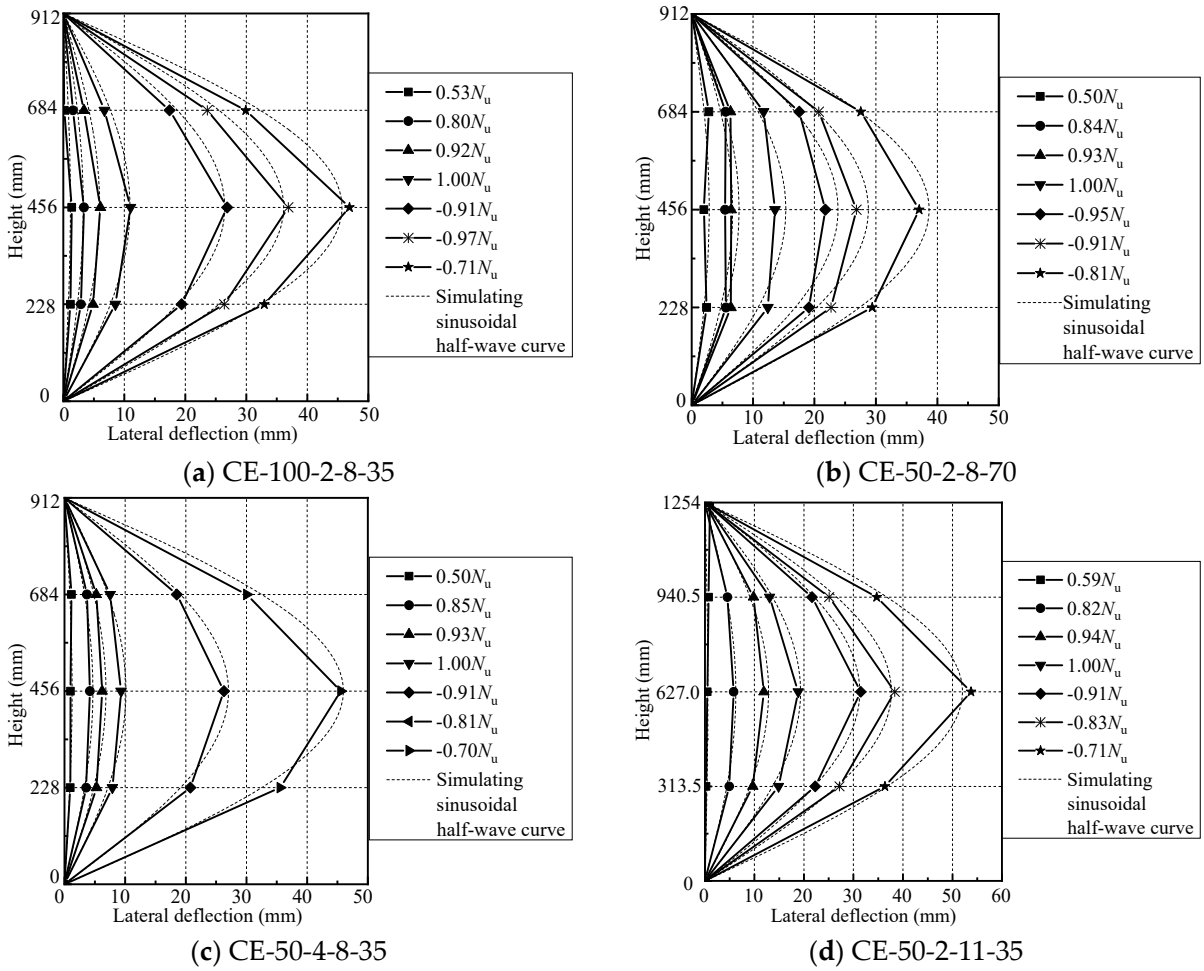

Figure 5. The distribution of lateral deflection along the column height in different load stages.

3.4. Stress–Strain Curve

The load–longitudinal strain relationship curve of C-BFRRACFST under the eccentric compression load is depicted in Figure 6. The core BFRRAC gradually forms a complicated three-dimensional compression state with increasing eccentric pressure during various

stress stages. Overall, the core BFRRAC was well constrained by the steel tube. This is due to the fact that when the C-BFRRACFST column attained the ultimate bearing capacity, the steel tube could provide sufficient constraint force to constrain the transverse deformation for core BFRRAC, so that the specimen's load–strain curve avoided a noticeable decline after reaching the ultimate bearing capacity.

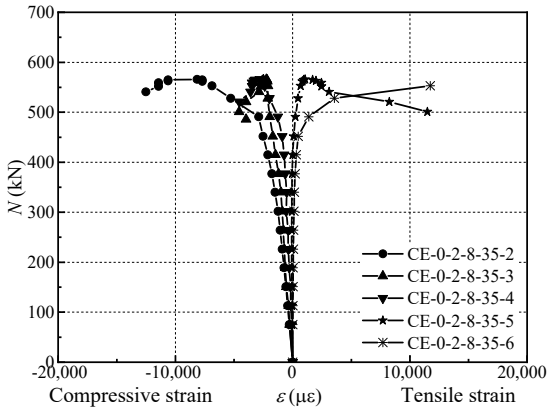

(**a**) CE-0-2-8-35

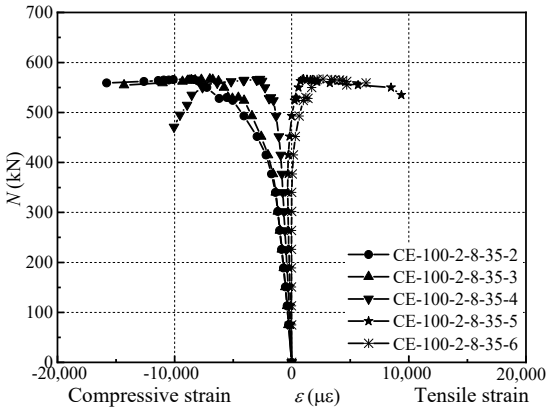

(**b**) CE-100-2-8-35

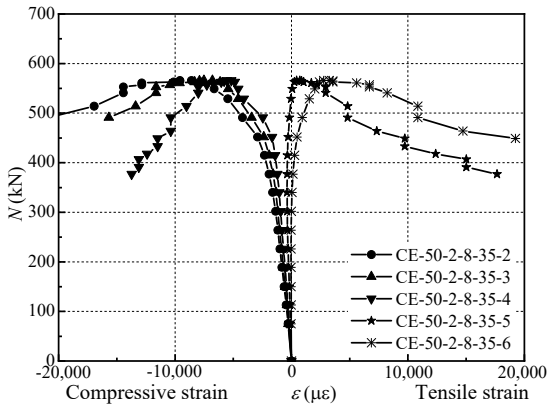

(**c**) CE-50-2-8-35

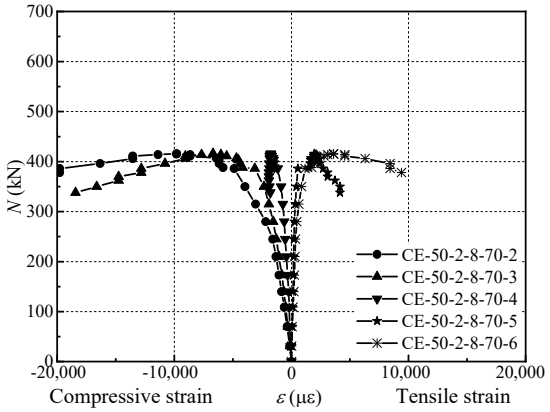

(**d**) CE-50-2-8-70

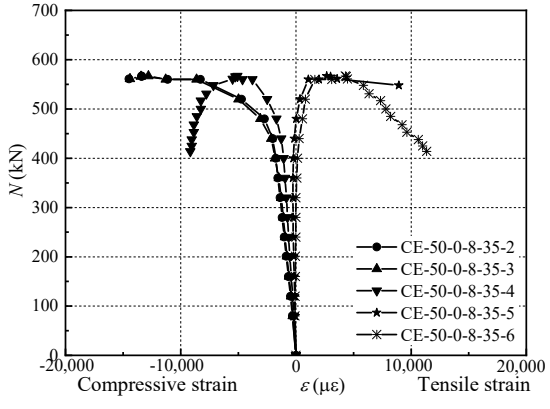

(**e**) CE-50-0-8-35

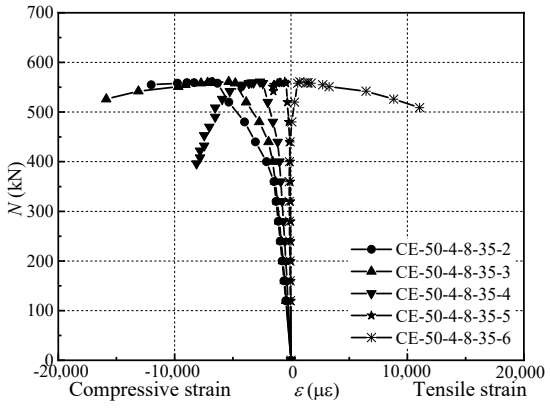

(**f**) CE-50-4-8-35

Figure 6. *Cont.*

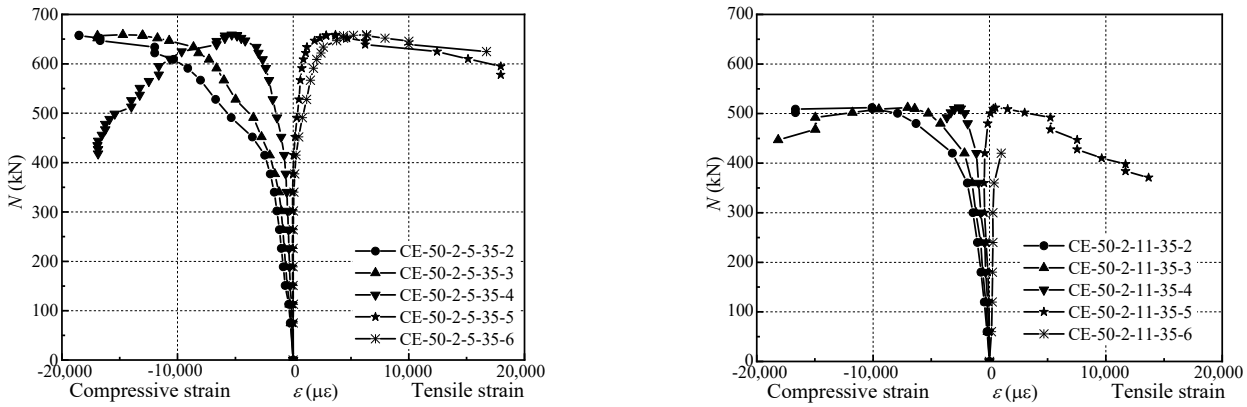

(**g**) CE-50-2-5-35 (**h**) CE-50-2-11-35

Figure 6. Load–longitudinal strain curve of eccentric compression specimen.

(1) Load–longitudinal strain curve

The strain gauge attached to the middle of the specimen could measure the longitudinal strain value for the eccentric compression specimen during the loading process. The load–longitudinal strain curve (N-ε) of the tensile and compressive zones of the C-BFRRACFST column is illustrated in Figure 6. Among them, 2~6 in the figure represent the number of five longitudinal strain gauges pasted in the specimen's mid-span, as well as the specific location, as shown in Figure 1c.

From Figure 6, when C-BFRRACFST column was destroyed, the section was partially pulled and compressed, and the steel tube approached yield strain. The No.5 and No.6 strain gauges were generally in the tensile state far away from eccentric load line, whereas the No.2 and No.3 strain gauges were generally in the compressive state.

During elastic stage, the specimen's load–longitudinal strain curve's slope change was somewhat different, and specimen CE-0-2-8-35 exhibited a longer elastic stage than other the specimens. After approaching the plastic stage, the slope of the curve gradually separated with the position of the strain gauge. The specimen's strain at this stage increased considerably when the replacement ratio of RCA was more than or equal to 50%, regardless of changes in the BF content, L/D, or eccentricity. Specimen CE-0-2-8-35′s strain gauges were destroyed after approaching the ultimate load, while the strains for other specimens continued to increase. This could be explained by the fact that RAC exhibited a lower compressive strength than concrete, and RCA also had initial damage. When the specimen was stressed, the microcracks in the internal RAC begin to develop, so that the steel tube was under a complex stress condition of longitudinal compression as well as earlier circumferential tension. After approaching the ultimate load, the deflection of the steel tube was fully developed, which caused serious local deformation and interfered with the strain gauge's ability to detect it. Therefore, only a handful of strain gauges can measure the load–longitudinal strain curve's declining section after the ultimate bearing capacity.

Comparing specimen CE-0-2-8-35 with specimen CE-100-2-8-35, it can be observed that specimen CE-100-2-8-35′s load–longitudinal strain curve's slope decreased slightly during the elastic–plastic stage, while after approaching the ultimate bearing capacity, the strain could still increase under the condition that the bearing capacity was not decreased considerably, that is, when the replacement ratios of RCA were 100%, the influence on specimen's deformation performance mainly occurred in the plastic stage. By contrasting specimen CE-50-2-8-35 and CE-50-2-8-70, it can be demonstrated that under an eccentricity of 35 mm, the specimen's load–longitudinal strain curve had a considerable slope during the elastic–plastic stage. After approaching the ultimate bearing capacity, the five strains increased rapidly with the decrease in bearing capacity. Comparing specimen CE-50-0-8-35 with CE-50-4-8-35, it was discovered that when the BF content was large, the declining stage of specimen's tensile zone was gentle, which demonstrates that BF's fracture resistance was mainly in the plastic stage. Comparing specimen CE-50-2-5-35 with specimen CE-50-

2-11-35, it was found that when the L/D was 11, the No.5 and No.6 strain gauge were destroyed when the specimens entered the elastic–plastic stage. When the L/D was 5, the specimen's strain increased fully in the plastic stage, indicating that the steel tube and the core BFRRAC work well together, the external steel tube was more evenly stressed, and that the steel tube performance was fully developed.

(2) Load–transverse strain curve

The measured load–transverse strain curve for the specimen is presented in Figure 7. Among them, the strain value of the load–transverse strain curve of the No.7 strain gauge in specimen CE-0-2-8-35, specimen CE-50-2-8-35, and specimen CE-50-2-11-35 was negative, indicating that the strain gauge was under compression from eccentric load. This is because under eccentric load, the specimens' tensile zone gradually extends longitudinally, and the corresponding transverse direction was transversely contracted, which caused the local area to be compressed. The slope of the same specimens' load–transverse strain curve was almost similar to that at the initial stage of loading. At this point, the core BFRRAC possessed no constraint by the steel tube. With the curve transformed from linear to non-linear, the micro-cracks inside the core BFRAC continued to develop, and the steel tube was squeezed horizontally. The core BFRRAC was circumferentially restrained from deforming by the steel tube, so that the core BFRRAC was in a complex stress state of three-dimensional compression. Meanwhile, the stress of the steel tube changed from longitudinal compression to circumferential tension. As the improvement in the eccentric compression load occurred, the circumferential tensile stress of the steel tube on the dangerous section first approach the yield strength value, and the surface of the steel tube was seriously buckled. When the specimen was destroyed, most of the area in the dangerous section was in the state of tensile yield. It can be observed that when subjected to eccentric compression load, the yield strength for steel tubes as well as the compressive strength for core concrete had significant factors to determine the specimen's elastic ultimate load, while the circumferential tensile strength for steel tubes show significant factors to determine the specimen's ultimate load.

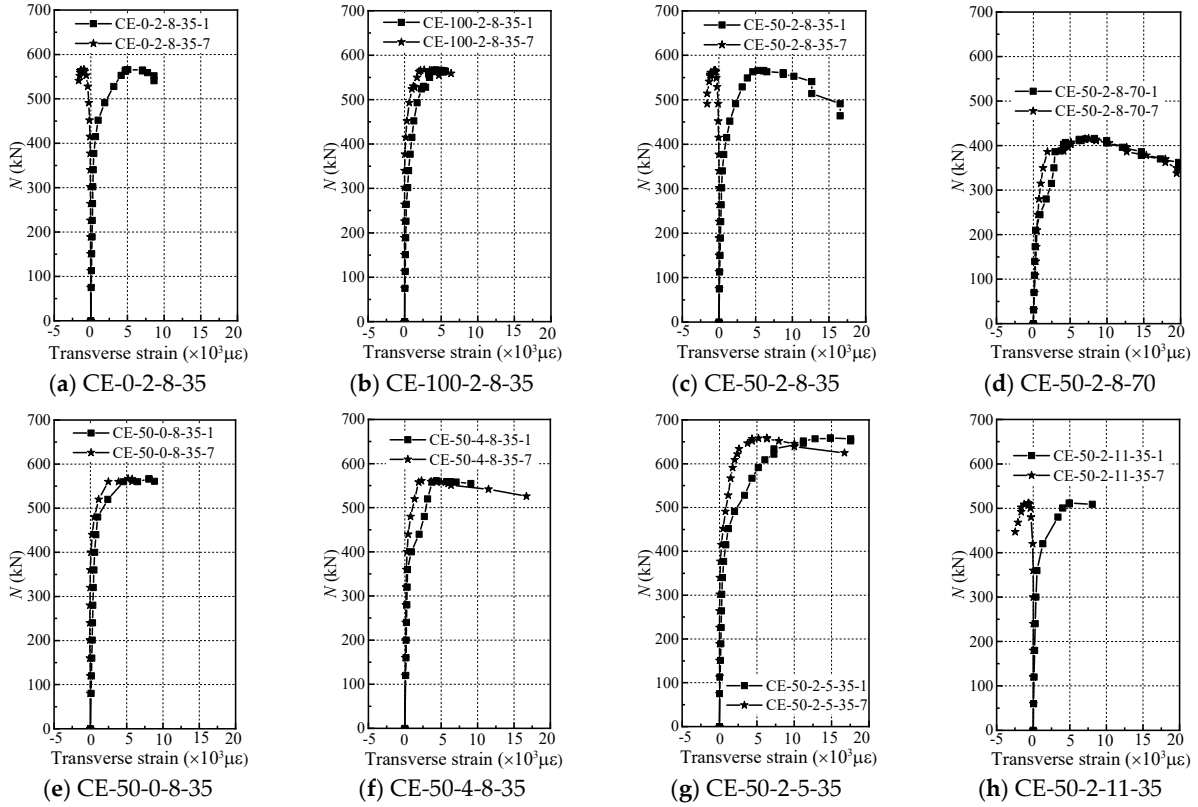

(**a**) CE-0-2-8-35 (**b**) CE-100-2-8-35 (**c**) CE-50-2-8-35 (**d**) CE-50-2-8-70

(**e**) CE-50-0-8-35 (**f**) CE-50-4-8-35 (**g**) CE-50-2-5-35 (**h**) CE-50-2-11-35

Figure 7. Load–transverse strain curve of specimen.

3.5. The Longitudinal Strain Distribution along the Height of the Middle Section of the Column

During various loading stages, the distribution curves of longitudinal strain along the height of the section in some specimens is illustrated from Figure 8. Among them, N_u is the specimen's measured ultimate load, the positive value of 0.90 N_u indicates the load level before the ultimate load, and the negative value of 0.99 N_u indicates the load level after the ultimate load. From Figure 8, the linear relationship of the specimen's mid-span section strain was more significant at the initial stage of loading, that is, the steel tube and BFRRAC work well together. While in the middle stage of loading, due to the influence of flexural deformation, and as the load gradually increases, the specimen's neutral axis continued to migrate toward the compression zone, and the strain distribution along the section height showed a nonlinear development. In general, in the different stages of eccentric compression loading in the C-BFRRACFST columns, the middle span of the column's cross-sectional strain progression primarily complied with the plane section assumption.

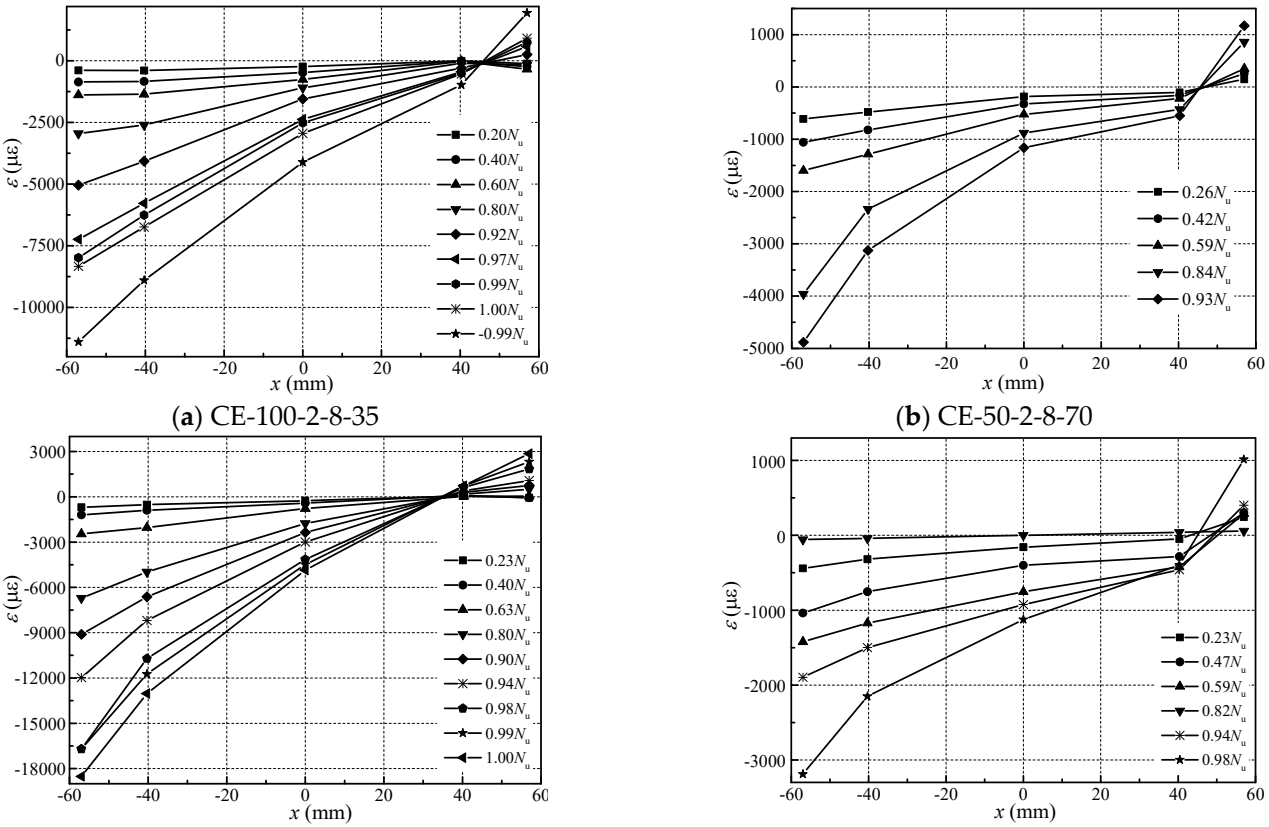

(**a**) CE-100-2-8-35 (**b**) CE-50-2-8-70

(**c**) CE-50-2-5-35 (**d**) CE-50-2-11-35

Figure 8. Longitudinal strain distribution along the height of the middle section of the column at different load stages.

3.6. Influence Analysis of Ultimate Bearing Capacity

Under eccentric compression load, the effect of various parameters upon the ultimate bearing capacity of the C-BFRRACFST column is depicted in Figure 9.

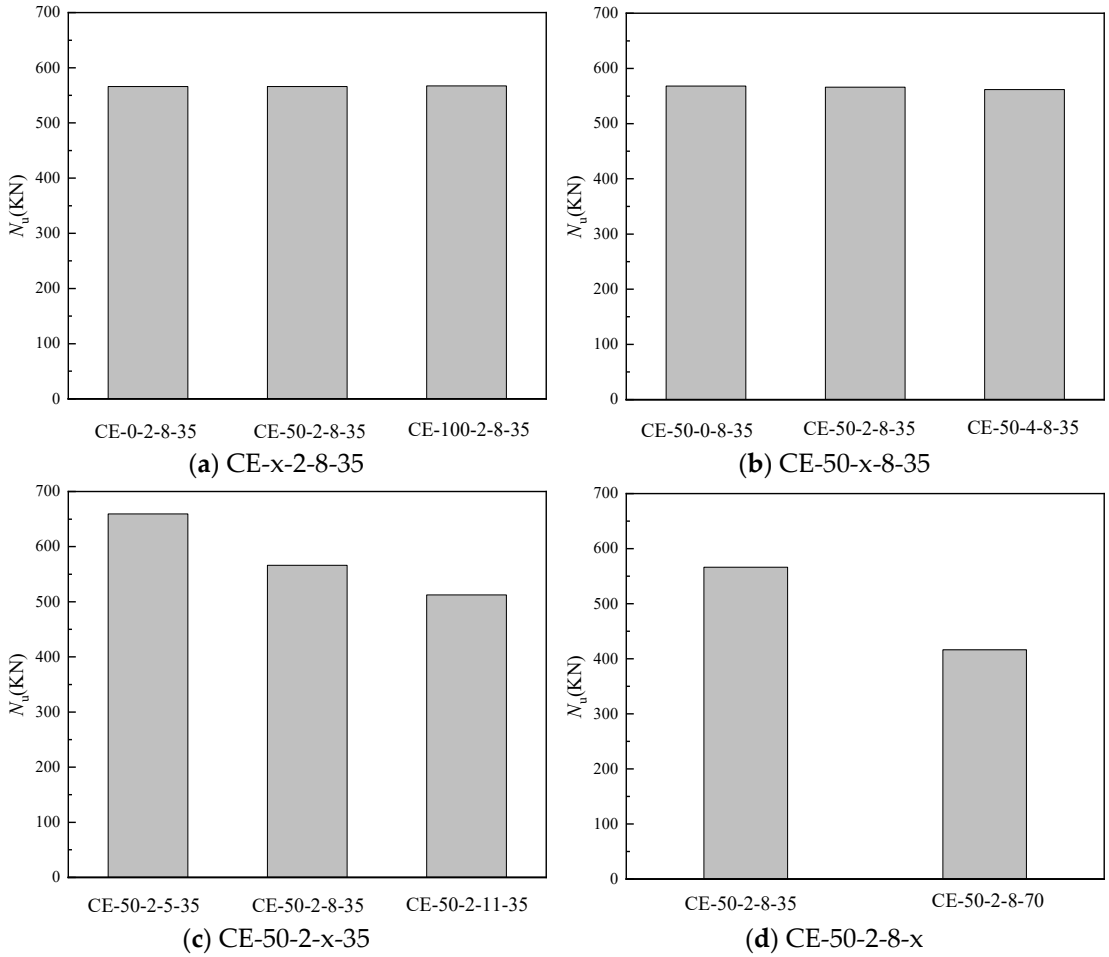

Figure 9. Effect of variable parameters on N_u.

(1) As illustrated in Figure 9a, under the condition of eccentric compression, and with the improvement for replacement ratios, the eccentric bearing capacity for the C-BFRRACFST columns nearly unaltered. That is, as the replacement ratio of RCA was 0%, although the compressive strength of the core BFRRAC under uniaxial compression load was higher, the overall bearing capacity of the C-BFRRACFST columns failed to demonstrate the advantages of its core BFRRAC.

(2) As seen in Figure 9b, increasing the BF content had little effect on the eccentric compression bearing capacity of the C-BFRRACFST column.

(3) As shown in Figure 9c, compared with specimen CE-50-2-8-35 with an L/D of 8, the ultimate bearing capacity for specimen CE-50-2-5-35 with an L/D of 5 increased by 16.44%, while the ultimate bearing capacity for specimen CE-50-2-11-35 with an L/D of 11 was reduced by 9.47%. This demonstrates that as the L/D increased, the ultimate bearing capacity of the C-BFRRACFST column gradually decreased.

(4) As demonstrated in Figure 9d, for the C-BFRRACFST column with an RCA replacement ratio of 50%, a BF content of 2 kg/m^3, an an L/D of 8, when the eccentricity was improved from 35 to 70 mm, the ultimate bearing capacity decreased by 26.47%. It can be observed that the ultimate bearing capacity for the C-BFRRACFST column progressively reduced with the improvement in eccentricity.

3.7. Ductility Coefficient

To study the effect of the replacement ratio of RCA, BF content, L/D, along with eccentricity on the ductility of C-BFRRACFST columns under eccentric compression load,

the ductility coefficient was calculated based on "Specification for seismic test of buildings" (China JGJ/T 101-2015 [33]), as shown in Equation (1).

$$\mu = \frac{\Delta_m}{\Delta_y} \tag{1}$$

where Δ_m represents the specimen's ultimate displacement, that is, the corresponding displacement as the load decreases to 85% of peak load after the load exceeded the ultimate load; Δ_y represents the specimen's yield displacement, that is, the corresponding displacement as the load rises to 75% of peak load.

The influence of various parameters on the ductility coefficient is shown in Figure 10.

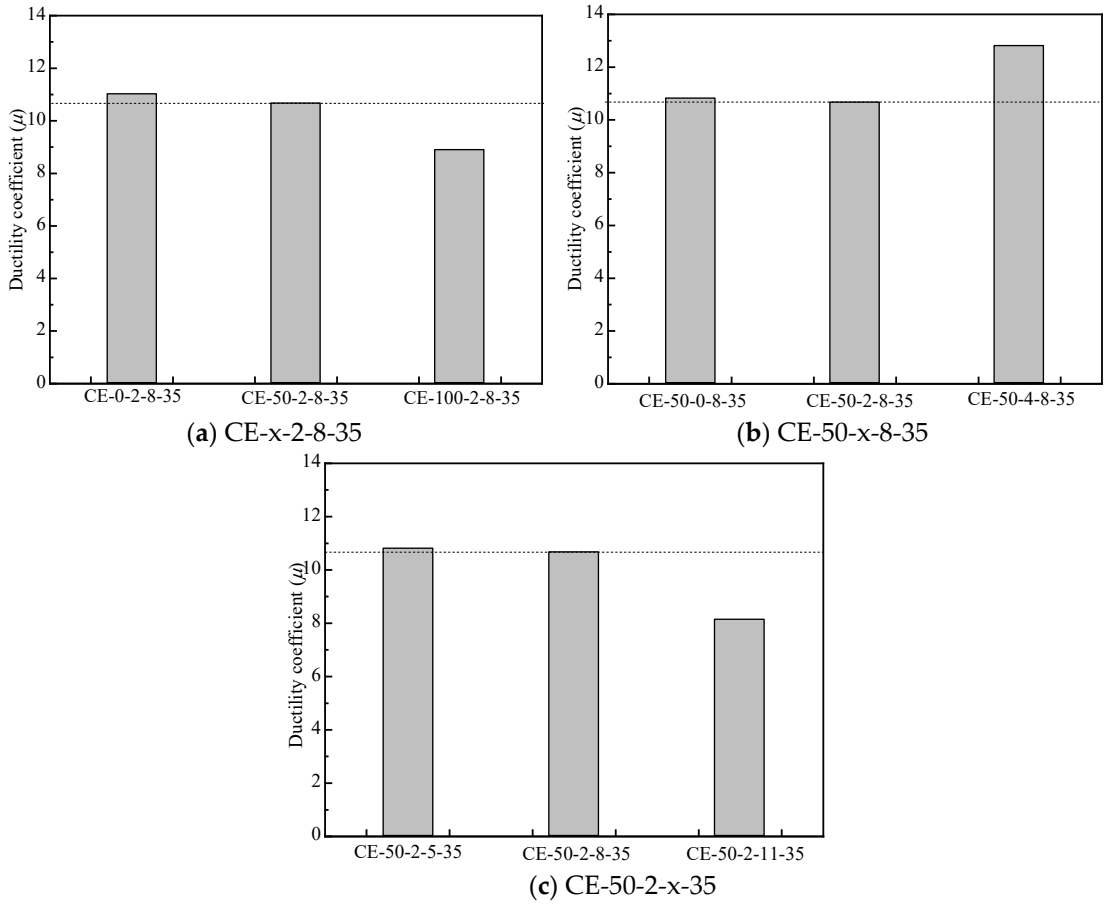

Figure 10. Comparison of ductility coefficient.

(1) From Figure 10a, the specimen's displacement ductility coefficient was concentrated in 8.89~11.02 under various replacement ratios of RCA. Compared with specimen CE-50-2-8-35, the displacement ductility coefficient of specimen CE-0-2-8-35 increased by 3.32%, while specimen CE-100-2-8-35 decreased by 16.65%; that is, the specimen's displacement ductility coefficient gradually decreased with the improvement in replacement ratios of RCA.

(2) The eccentric compression displacement ductility coefficient of the C-BFRRACFST column was displayed through Figure 10b with various BF contents, and it can be observed that the specimen's displacement ductility coefficient was concentrated between 10.67 and 12.81. Compared with specimen CE-50-2-8-35, the displacement ductility coefficient of specimen CE-50-0-8-35 increased by 1.40%, with a small increase, while specimen CE-50-4-8-35 increased by 20.10%; that is, increasing the BF content can considerably increase the specimen's displacement ductility coefficient.

(3) The C-BFRRACFST column's eccentric compression displacement ductility coefficient under various L/D is presented in Figure 10c, where it can be observed that the specimen's displacement ductility coefficient was concentrated between 8.13 and 1.81. Compared with specimen CE-50-2-8-35, the displacement ductility coefficient of specimen CE-50-2-5-35 increased by 1.31%, while specimen CE-50-2-11-35 decreased by 23.80%, which is a large reduction; that is, the specimen's displacement ductility coefficient gradually decreased with the increase in L/D.

4. Finite Element Analysis of Circular Steel Tube Basalt Fiber Recycled Concrete Column

4.1. Constitutive Relation

The steel's constitutive model adopted the bilinear model of a uniaxial stress–strain curve. The elastoplastic materials' constitutive relationship, comprising the elastic stage as well as the strengthening stage, is represented by two straight lines in the model. The elastic modulus of the plastic strengthening stage can be approximated by 0.01 E_s (E_s indicates the steel's elastic modulus). The constitutive relation of concrete was determined according to the relevant research results of the research group [34].

4.2. Establishment of ABAQUS Model

The 8-node hexahedral linear reduced integral unit (C3D8R) was selected for the core BFRAC. The 4-node quadrilateral linear reduced integral shell element (S4R) was selected for the outer steel tube as well as the end cover plate. The thickness integration rule utilized Simpson, and the thickness integration point was 5. The cover plate was configured as a rigid material that had large stiffness, and the material property was configured to be elastic. The cover plate's elastic modulus was 1000 times that of the steel utilized, and the Poisson's ratio was set to 0.3. The "hard contact" model was employed for the normal contact, and the Coulomb friction model was utilized for the tangential contact. In addition, the steel tube and the BFRRAC had a contact friction coefficient of 0.6. The contact interface between the inner surface of the end plate and the steel tube and the contact of BFRRAC were all constrained by Tie in the Constraint command.

Once the boundary conditions were defined, the loading point as well as support at both ends were defined as the reference point. The reference point as well as the corresponding outer surface of the cover plate were constrained by Coupling, the load was applied to the reference point, and the load was transmitted to the cover plate through the reference point. The boundary conditions of the C-BFRRACFST column's finite element model under eccentric compression are illustrated in Figure 11.

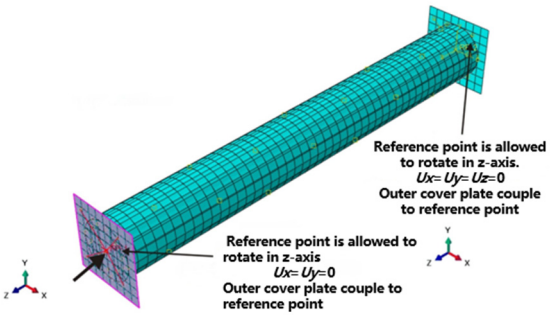

Figure 11. Boundary conditions of finite element model of specimen.

4.3. Finite Element Simulation Analysis

4.3.1. Comparative Analysis of ABAQUS Results

The eccentric compression of the C-BFRRACFST column was simulated by using the above material's constitutive relationship and the finite element model establishment method. In addition, the finite element simulation load–axial displacement curve was compared with the experimentally measured curve, as demonstrated in Figure 12.

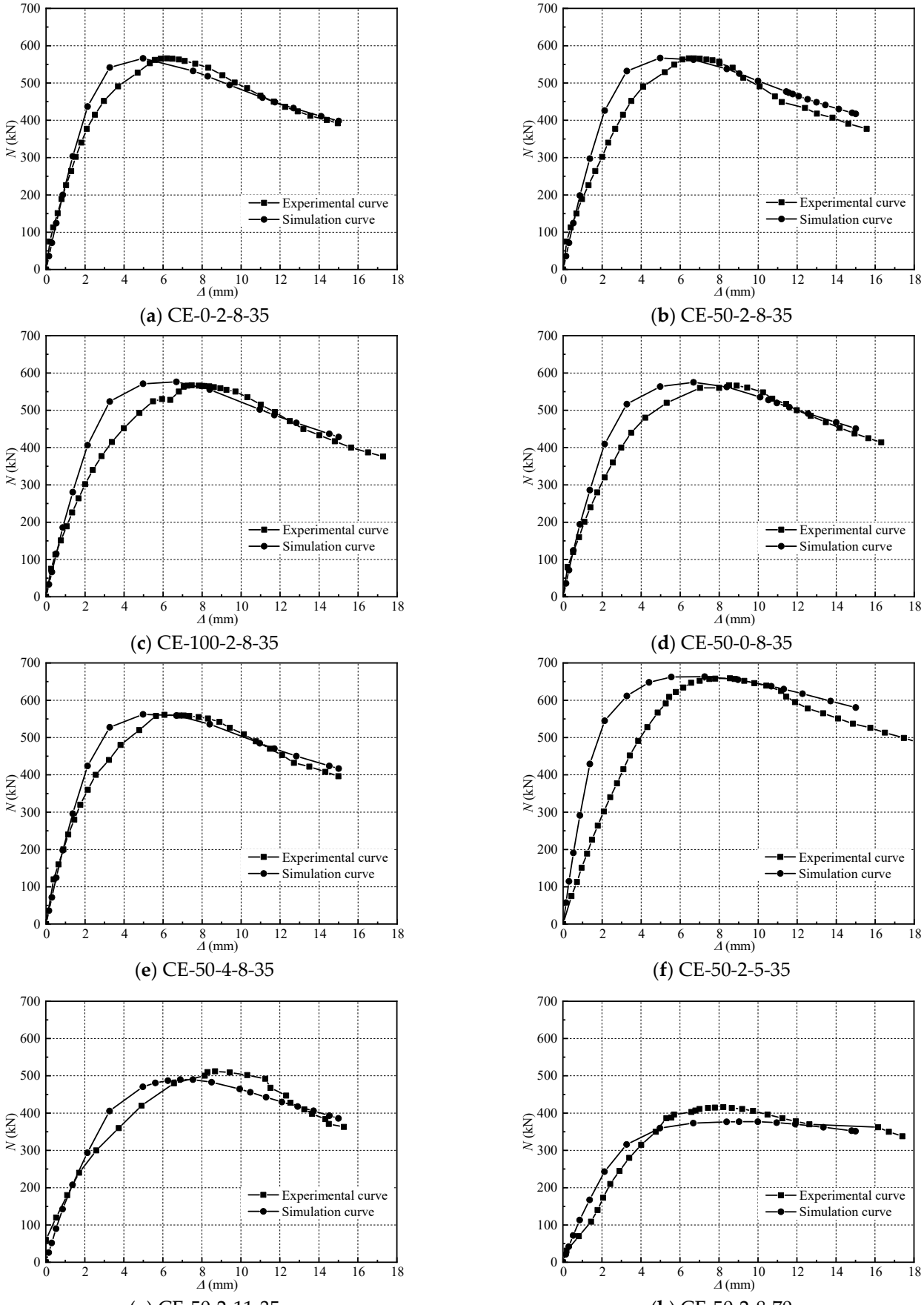

(**a**) CE-0-2-8-35 (**b**) CE-50-2-8-35

(**c**) CE-100-2-8-35 (**d**) CE-50-0-8-35

(**e**) CE-50-4-8-35 (**f**) CE-50-2-5-35

(**g**) CE-50-2-11-35 (**h**) CE-50-2-8-70

Figure 12. Comparison of test results and simulation results of eccentric compression.

As demonstrated in Figure 12, under eccentric compression stress, the simulated specimen's ultimate bearing capacity was marginally higher than that of the experimental specimen. However, the ultimate bearing capacity for certain simulated specimens was lower. This could be explained by the slight discrepancy between the designed initial eccentricity and the actual eccentricity during the test, which caused the difference in the ultimate bearing capacity between experimental specimen and simulated specimen.

The specimen's ultimate bearing capacity between the finite element calculation value N_e and the test measured value N_u are exhibited in Table 4. Under eccentric compression load, the C-BFRRACFST column's ultimate bearing capacity which was simulated by the ABAQUS finite element was close to experimental bearing capacity. The mean value of the ratio was 1.014 and the variance was 0.002.

Table 4. Comparison of finite element calculation values of ultimate bearing capacity of specimens under eccentric compression with experimental measured values.

Specimen Number	L (mm)	N_u (kN)	N_e (kN)	M_u (kN m)	N_u/N_e
CE-0-2-8-35	912	566.04	566.21	19.82	1.000
CE-100-2-8-35	912	567.07	576.19	20.17	0.984
CE-50-2-8-35	912	566.22	567.05	19.85	0.999
CE-50-2-8-70	912	416.29	377.08	26.40	1.104
CE-50-0-8-35	912	568.01	575.03	20.13	0.988
CE-50-4-8-35	912	561.85	562.29	19.68	0.999
CE-50-2-5-35	570	659.33	663.34	23.22	0.994
CE-50-2-11-35	1254	512.59	489.96	17.15	1.046

The simulation curves can be divided into increasing and declining sections. The slope of the increasing section was a little larger than that of the experimental curve, and the declining section showed good agreement. In summary, the finite element model developed during this study can better reflect the eccentric compression performance of C-BFRRACFST columns and can also validate the correctness of the ABAQUS finite element model selected during this study as well as the feasibility of the analysis method.

4.3.2. Analysis of Influence Factors of Eccentricity

One of the crucial elements which we recommend to be considered in practical engineering applications is the connection between the specimen's bearing capacity and the eccentricity. However, the number of specimens in this experiment was limited, and the consequence of modifying the eccentricity upon the specimen's bearing performance was not sufficiently taken into account. It could not fully meet the needs of engineering structures. Therefore, based on the existing finite element simulation results, the ABAQUS finite element models were established for various eccentricities such as 10, 20, 35, 50, 70, 83, 90, 110, 150, 200, 300 mm, and 500 mm; soon afterwards, the specimen's ultimate bearing capacity was obtained. Eight groups of finite element models' load–axial displacement curves for each operating condition are represented from Figure 13. As can be observed, the specimen's ultimate bearing capacity and the elastic section stiffness considerably decreased as eccentricity improved.

4.3.3. Bearing Capacity Correlation Equation of Compression-Bending Member

Currently, there are relevant reports on the calculation model of the bearing capacity of confined concrete [35]. Combined with the research object of this study, the typical N/Nu-M/Mu strength curve of concrete-filled steel tubular (CFST) flexural members is illustrated in Figure 14. Based on the simulation results, the N/Nu-M/Mu strength relationship of the C-BFRRACFST column was derived, and the relevant calculation formula was obtained. To confirm the degree of agreement, the formula calculation results were compared with the ABAQUS simulation results presented in Figure 13.

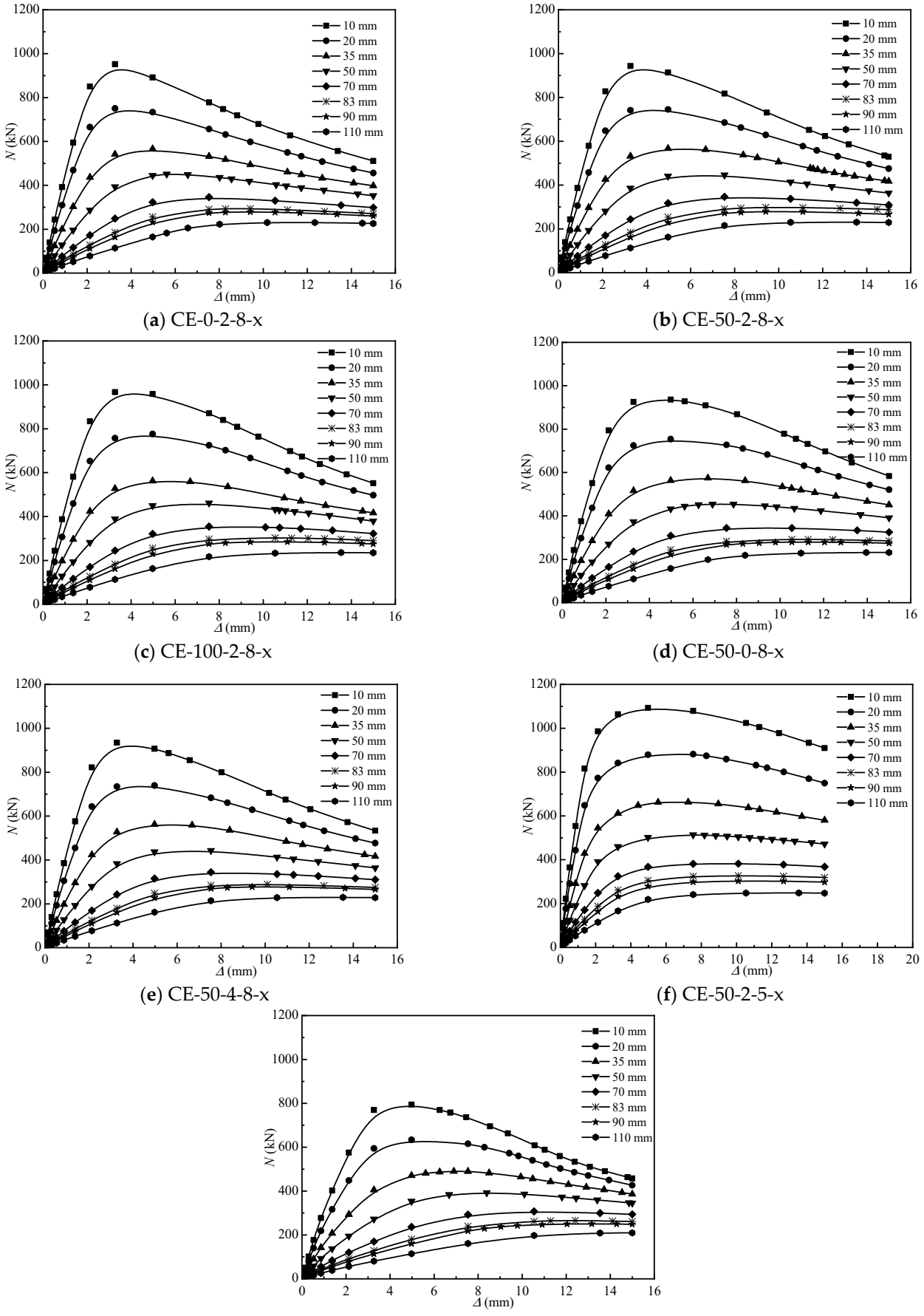

(**a**) CE-0-2-8-x

(**b**) CE-50-2-8-x

(**c**) CE-100-2-8-x

(**d**) CE-50-0-8-x

(**e**) CE-50-4-8-x

(**f**) CE-50-2-5-x

(**g**) CE-50-2-11-x

Figure 13. Load-axial displacement curves under different eccentricity.

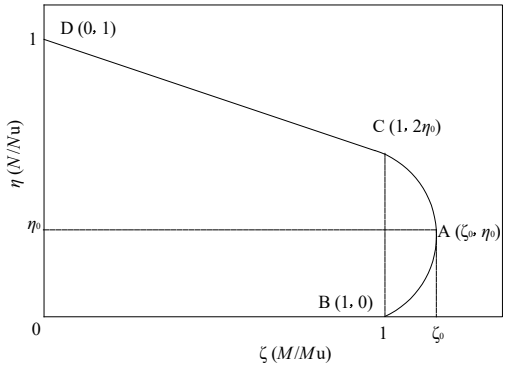

Figure 14. Typical N/Nu–M/Mu intensity relation curve.

The mechanical properties of the C-BFRRACFST columns were similar to the CFST flexural members. In addition, there also existed a large and small eccentric compression equilibrium point A (as shown in Figure 14) on the N/Nu-M/Mu strength relation curve, which was called A (ζ_0, η_0) in coordinate axis. Since all of the specimens' cross sections in this study were circular, the expressions of ζ_0 and η_0 were obtained by consulting the reference [36] and modifying the coefficients, as demonstrated in Equations (2) and (3).

$$\zeta_0 = 0.98 + 0.14\xi^{-1.15} \tag{2}$$

$$\eta_0 = 0.17 + 0.144\xi^{-0.84} \tag{3}$$

According to the method provided in reference [36], taking into account the effect of L/D on the C-BFRRACFST column and the second-order bending moment, the relationship equation of N/Nu-M/Mu can be summarized as:

$$\begin{cases} \frac{1}{\varphi} \cdot \left(\frac{N}{N_u}\right) + \frac{a}{d} \cdot \left(\frac{M}{M_u}\right) = 1 & \left(N/N_u \geq 2\varphi^3 \cdot \eta_0\right) \\ -b \cdot \left(\frac{N}{N_u}\right)^2 - c \cdot \left(\frac{N}{N_u}\right) + \frac{1}{d} \cdot \left(\frac{M}{M_u}\right) = 1 & \left(N/N_u < 2\varphi^3 \cdot \eta_0\right) \end{cases} \tag{4}$$

where $1/d$ represents the amplification factor of bending moment caused by the second-order effect. Furthermore, the calculation methods of a, b, c, and d are shown in Equations (5)–(8).

$$a = 1 - 2\varphi^2 \cdot \eta_0 \tag{5}$$

$$b = \frac{1 - \zeta_0}{\varphi^3 \times \eta_0^2} \tag{6}$$

$$c = \frac{2 \cdot (\zeta_0 - 1)}{\eta_0} \tag{7}$$

$$d = 1 - 0.4 \cdot \left(\frac{N}{N_E}\right) \tag{8}$$

The calculation method of Euler's critical force N_E was demonstrated in Equations (9)–(13).

$$N_B = \frac{\pi^2 \cdot E_{sc} \cdot A_{sc}}{\lambda^2} \tag{9}$$

$$E_{sc} = f_{scp}/\varepsilon_{scp} \tag{10}$$

$$f_{scp} = \left[0.192\left(f_y/235\right) + 0.488\right] \cdot f_{scy} \tag{11}$$

$$\varepsilon_{scp} = 3.25 \times 10^{-6} f_y \tag{12}$$

$$f_{scy} = (1.14 + 1.02\xi) \cdot f_{ck} \tag{13}$$

where: f_{scp}—proportional limit of the specimen under axial compression;

f_{scy}—strength index of the specimen under axial compression;

E_{sc}—elastic modulus of the specimen under axial compression;

A_{sc}—the cross-sectional area of the specimen's whole section (mm), Asc = As + Ac;

f_{ck}—the design value of the compressive strength of core concrete (MPa)

The research group's previous findings indicate that error modification can be performed by multiplying the coefficient ψ [37], and the procedure for calculating the correction coefficient is provided in Equation (14).

$$\psi = (0.028m_{BF} - 0.26)\gamma^2 + (-0.03m_{BF} + 0.32)\gamma + \left(-0.01m_{BF}^2 + 0.036m_{BF} + 1.046\right) \tag{14}$$

Therefore, the calculation method for he C-BFRRACFST short column's axial compression bearing capacity is illustrated in Equation (15).

$$N_v = \psi \cdot A_{sc} \cdot f_{scy} \tag{15}$$

φ is the bearing capacity reduction factor of C-BFRRACFST column, taking into consideration the influence of slenderness ratio, which is determined by Equation (16).

$$\varphi = \begin{cases} 1 & (\lambda \le \lambda_0) \\ a \cdot \lambda^2 + b \cdot \lambda + c & (\lambda_0 < \lambda \le \lambda_p) \\ d/(\lambda + 35)^2 & (\lambda > \lambda_p) \end{cases} \tag{16}$$

Among them,

$$\lambda_0 = \pi\sqrt{(420\xi + 550)/[(1.02\xi + 1.14) \cdot f_{ck}]} \tag{17}$$

$$\lambda_p = 1743/\sqrt{f_y} \tag{18}$$

$$a = \frac{1 + (35 + 2 \cdot \lambda_p - \lambda_0) \cdot e}{(\lambda_p - \lambda_0)^2} \tag{19}$$

$$b = e - 2 \cdot a \cdot \lambda_p \tag{20}$$

$$c = 1 - a \cdot \lambda_0^2 - b \cdot \lambda_0 \tag{21}$$

$$d = \left[13000 + 4657 \cdot \ln\left(\frac{235}{f_y}\right)\right] \cdot \left(\frac{25}{f_{ck} + 5}\right)^{0.3} \cdot \left(\frac{\alpha}{0.1}\right)^{0.05} \tag{22}$$

$$e = \frac{-d}{(\lambda_p + 35)^3} \tag{23}$$

where: ψ—the specimen's bearing capacity correction coefficient considering the incorporation of BF;

λ_p—the axial compression specimen's ultimate L/D when elastic instability occurs;

λ_0—the axial compression specimen's ultimate L/D when elastic–plastic instability occurs;

α—steel ratio of the section, $\alpha = A_s/A_c$.

Therefore, the calculation method for the stable compressive bearing capacity of the C-BFRRACFST column is demonstrated in Equation (24).

$$N_{u,cr} = \varphi \cdot Nu = \varphi \cdot \psi \cdot A_{sc} \cdot f_{scy} \tag{24}$$

The calculation method of flexural strength bearing capacity of C-BFRRACFST column is shown in Equation (25).

$$M_u = \gamma_m \cdot f_{scy} \cdot W_{scm} \quad (25)$$

$$W_{scm} = \pi D^3/32 \quad (26)$$

where W_{scm} indicates the specimen's flexural section modulus, and the calculation method is provided in Equation (26). γm indicates the calculation coefficient for the modified bending strength bearing capacity, and Equation (27) demonstrates the calculation process.

$$\gamma_m = 1.64 + 0.34 \ln(\xi, + 0.1) \quad (27)$$

The parameters were brought into the aforementioned equation, and the *N*/*Nu*-*M*/*Mu* correlation curve of the C-BFRRACFST column was eventually generated, which is demonstrated in Figure 15. The bearing capacity calculated by the aforementioned equation is similar to the finite element simulation value in Figure 13, indicating a significant amount of coincidence between the two. Therefore, the modified *N*/*Nu*-*M*/*Mu* correlation curve equation in this study has broad application and should be considered for utilization in related engineering design.

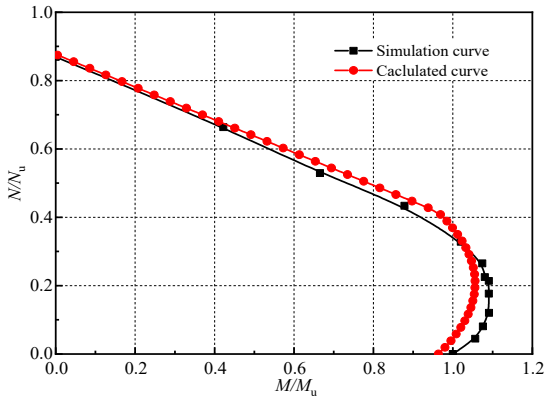

(**a**) CE-0-2-8-x

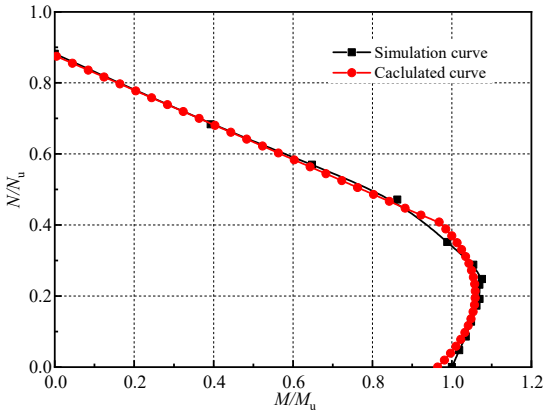

(**b**) CE-50-2-8-x

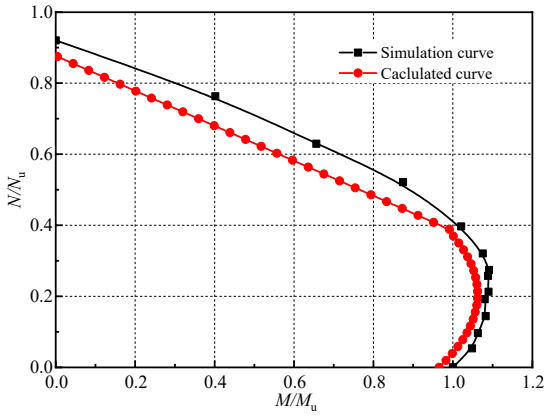

(**c**) CE-100-2-8-x

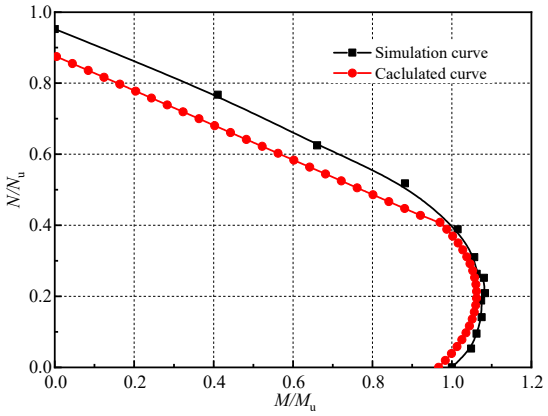

(**d**) CE-50-0-8-x

Figure 15. *Cont.*

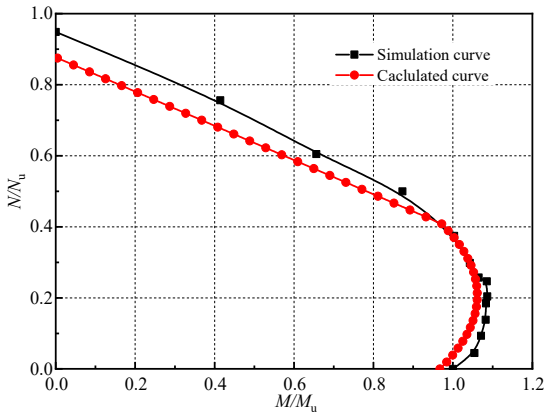

(**e**) CE-50-4-8-x

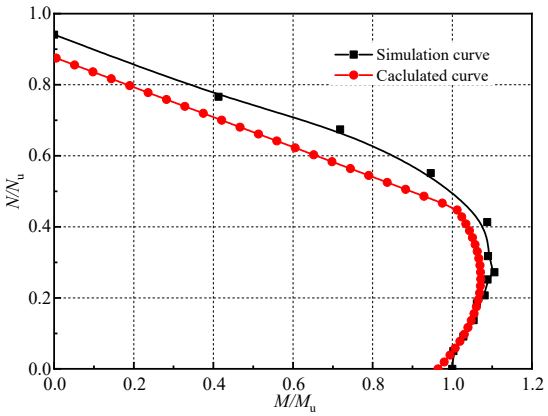

(**f**) CE-50-2-5-x

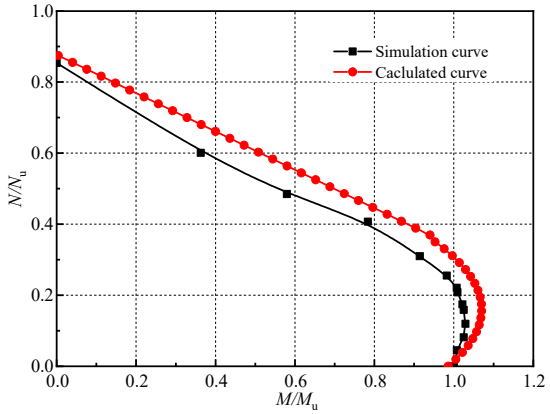

(**g**) CE-50-2-11-x

Figure 15. Comparison of *N*/*Nu*-*M*/*Mu* curves.

5. Conclusions

Within the parameters of the design, the eccentric compression test and finite element analysis of eight C-BFRRACFST columns were performed in this work. The following are the primary conclusions.

(1) Under eccentric compression load, in the specimens with an L/D of 8 and 11, the final failure mode was bending failure caused by the global buckling of the steel tube; for the specimens with an L/D of 5, the final failure mode was bending failure caused by the the interaction between global buckling and local buckling.

(2) At different stages of eccentric compression loading, the C-BFRRACFST column's mid-span section strain primarily complied with the plane section assumption, and the lateral deflection along the column height distribution basically conformed to the sinusoidal half-wave curve.

(3) Under the eccentric compression load, the replacement ratio of RCA and BF content had little effect on the peak load of the specimen. With the increase in L/D, the peak load and ductility were significantly reduced. Increasing the BF content can significantly improve the ductility. The increase in eccentricity also has a significant adverse effect on the peak load.

(4) The finite element model established during this study better reflects the eccentric compression performance of the C-BFRRACFST column. Through the finite element analysis of the eccentricity-influencing factors, the specimens' ultimate bearing capacity under various eccentricity was obtained. The specimen's ultimate bearing capacity and the elastic stiffness considerably decreased as eccentricity improved.

(5) Based on the existing calculation equation of CFST, the calculation equation for the stable compressive bearing capacity of the C-BFRRACFST column is presented, and the N/N_u-M/M_u correlation curve equation is modified. The calculation results demonstrate close alignment with the finite element simulation results and provide reference for the related design and application in engineering construction.

In summary, this study investigated the eccentric compression mechanical properties of eight C-BFRRACFST columns. However, due to factors such as test conditions, this study only analyzes a single specimen under different changing parameters. Through the finite element model, the influence of more eccentricity on the bearing capacity of the specimen was explored. At present, there are few studies on the mechanical properties of C-BFRRACFST. In the future, our research group will draw lessons from and compare with other researchers' related research, and in time supplement and verify the current research conclusions of our research group. At the same time, our research group will study the durability, seismic performance, and impact resistance of C-BFRRACFST under different parameters such as different wall thicknesses of steel tubes and basalt fiber types in the future.

Author Contributions: Conceptualization, Y.F. and S.Q.; methodology, X.Z. and Y.F.; software, X.K. and C.L.; validation, J.N. and S.Q.; formal analysis, J.N. and C.L.; investigation, J.N.; data curation, X.Z.; writing—original draft preparation, X.Z.; writing—review and editing, Y.F.; visualization, Y.H.; supervision, X.K. All authors have read and agreed to the published version of the manuscript.

Funding: This work was supported by the Funds for Establishment Project of Double First-Class Disciplines of Safety and Energy Engineering Department (AQ20230731, AQ20230736), the National Natural Science Foundation of China through contracts (52274077), the Fundamental Research Funds for the Universities of Henan Province (NSFRF220440), the Funds for Distinguished Young Scholars of Henan Polytechnic University (J2023-3), Key Scientific Research Projects of Colleges and Universities in Henan Province (23A560008) and Henan Province National Science Foundation (222300420446).

Institutional Review Board Statement: We did not perform human research and do not require ethical approval.

Informed Consent Statement: We did not perform human research.

Data Availability Statement: The data used to support the findings of this study are included within the article.

Conflicts of Interest: The authors declare no conflict of interest.

References

1. Bian, J.W.; Zhang, W.B.; Shen, Z.Z.; Li, S.; Chen, Z.L. Analysis and optimization of mechanical properties of recycled concrete based on aggregate characteristics. *Sci. Eng. Compos. Mater.* **2021**, *28*, 516–527. [CrossRef]
2. Ahmadi, M.; Farzin, S.; Hassani, A.; Motamedi, M. Mechanical properties of the concrete containing recycled fibers and aggregates. *Constr. Build. Mater.* **2017**, *144*, 392–398. [CrossRef]
3. Li, Y.S.; Zhang, X.Q.; Ding, G.Y.; Feng, Z.Q. Developing a quantitative construction waste estimation model for building construction projects. *Resour. Conserv. Recycl.* **2016**, *106*, 9–20. [CrossRef]
4. Kim, J. Construction and demolition waste management in Korea: Recycled aggregate and its application. *Clean Technol. Environ. Policy* **2021**, *23*, 2223–2234. [CrossRef]
5. Sharma, R. Laboratory Study on effect of construction wastes and admixtures on compressive strength of concrete. *Arab. J. Sci. Eng.* **2017**, *42*, 3945–3962. [CrossRef]
6. Wang, Y. Simulation study on the effect of the initial defect of recycled aggregate concrete based on BFEM. *Constr. Build. Mater.* **2022**, *355*, 129219. [CrossRef]
7. Kim, J. Influence of quality of recycled aggregates on the mechanical properties of recycled aggregate concretes: An overview. *Constr. Build. Mater.* **2022**, *328*, 127071. [CrossRef]
8. Tam, V.W.Y.; Wattage, H.; Le, K.N.; Buteraa, A.; Soomro, M. Methods to improve microstructural properties of recycled concrete aggregate: A critical review. *Constr. Build. Mater.* **2020**, *270*, 121490. [CrossRef]
9. Gou, M.H.; Gong, G.Q.; Yue, Y.C.; Xing, F.; Zhou, Y.W.; Hu, B. Performance evaluation of recycled aggregate concrete incorporating limestone calcined clay cement (LC3). *J. Clean. Prod.* **2022**, *366*, 132820. [CrossRef]

10. Jiang, Y.J.; Li, B.; He, J.; Hernandez, A.G. Properties and microstructure of packing-optimised recycled aggregate concrete with different cement paste or sand contents. *Constr. Build. Mater.* **2022**, *344*, 128178. [CrossRef]
11. Li, L.; Xuan, D.X.; Sojobi, A.O.; Liu, S.H.; Poon, C.S. Efficiencies of carbonation and nano silica treatment methods in enhancing the performance of recycled aggregate concrete. *Constr. Build. Mater.* **2021**, *308*, 125080. [CrossRef]
12. Niu, H.C.; Cao, W.L. Full-scale testing of high-strength RACFST columns subjected to axial compression. *Mag. Concr. Res.* **2015**, *67*, 257–270. [CrossRef]
13. Li, J.T.; Chen, Z.P.; Xu, J.J.; Jing, C.G.; Xue, J.Y. Cyclic behavior of concrete-filled steel tubular column–reinforced concrete beam frames incorporating 100% recycled concrete aggregates. *Adv. Struct. Eng.* **2018**, *21*, 1802–1814. [CrossRef]
14. Chen, J.; Zhang, S.M.; Wang, Y.Y.; Geng, Y. Axial compressive behavior of recycled concrete filled steel tubular stub columns with the inclusion of crushed brick. *Structures* **2020**, *26*, 271–283. [CrossRef]
15. Liu, Y.C.; Lyu, F.; Ding, F.X.; Wang, E.; Xu, Y.L.; Yuan, T.; Deng, C.; Luo, C. Numerical study on confinement effect and efficiency of concentrically loaded RACFRST stub columns. *Front. Mater.* **2021**, *8*, 630774. [CrossRef]
16. Yang, Y.F.; Hou, C. Behaviour and design calculations of recycled aggregate concrete-filled steel tube (RACFST) members. *Mag. Concr. Res.* **2015**, *67*, 611–620. [CrossRef]
17. Chen, Z.P.; Jing, G.G.; Xu, J.J.; Zhang, X.G. Seismic performance of recycled concrete-filled square steel tube columns. *Earthq. Eng. Eng. Vib.* **2017**, *16*, 119–130. [CrossRef]
18. Liu, F.; Yu, Y.Y.; Li, L.J.; Zeng, L. Experimental study on reuse of recycled concrete aggregates for load-bearing components of building structures. *J. Mater. Cycles Waste Manag.* **2017**, *20*, 995–1005. [CrossRef]
19. Huang, Y.J.; Xiao, J.Z.; Shen, L.M. Damage assessment for seismic response of recycled concrete filled steel tube columns. *Earthq. Eng. Eng. Vib.* **2016**, *15*, 607–616. [CrossRef]
20. Jin, X. Analysis the nonlinear finite element of bearing capacity of recycled concrete filled steel tubular columns. *Agro Food Ind. Hi-Tech* **2017**, *28*, 747–751.
21. Dong, J.F.; Wang, Q.Y.; Guan, Z.W. Material properties of basalt fibre reinforced concrete made with recycled earthquake waste. *Constr. Build. Mater.* **2017**, *130*, 241–251. [CrossRef]
22. Zheng, Y.X.; Zhou, J.B.; Zhang, P.; Ma, M. Mechanical properties and meso-microscopic mechanism of basalt fiber-reinforced recycled aggregate concrete. *J. Clean. Prod.* **2022**, *370*, 133555. [CrossRef]
23. Liu, K.N.; Wang, S.L.; Quan, X.Y.; Duan, W.; Nan, Z.; Wei, T.; Xu, F.; Li, B.B. Study on the mechanical properties and microstructure of fiber reinforced metakaolin-based recycled aggregate concrete. *Constr. Build. Mater.* **2021**, *294*, 123554. [CrossRef]
24. Li, S.; Zhang, Y.; Chen, W. Bending performance of unbonded prestressed basalt fiber recycled concrete beams. *Eng. Struct.* **2020**, *221*, 110937. [CrossRef]
25. Huang, M.; Zhao, Y.R.; Wang, H.N.; Lin, S.H. Mechanical properties test and strength prediction on basalt fiber reinforced recycled concrete. *Adv. Civ. Eng.* **2021**, *2021*, 6673416. [CrossRef]
26. Du, X.Q.; Li, Y.L.; Si, Z.; Huang, L.Z.; Chen, X.G. Effects of basalt fiber and polyvinyl alcohol fiber on the properties of recycled aggregate concrete and optimization of fiber contents. *Constr. Build. Mater.* **2022**, *340*, 127646. [CrossRef]
27. Katkhuda, H.; Shatarat, N. Improving the mechanical properties of recycled concrete aggregate using chopped basalt fibers and acid treatment. *Constr. Build. Mater.* **2017**, *140*, 328–335. [CrossRef]
28. Shatarat, N.; Katkhuda, H.; Ayyoub, M.; Al-Hunaiti, Y.; Jaber, M.S.A. Improving bond strength of recycled coarse aggregate concrete using chopped basalt fibers. *Case Stud. Constr. Mater.* **2022**, *17*, e01449. [CrossRef]
29. Hafsa, J.; Rajesh, M. A green material from rock: Basalt fiber—A review. *J. Text. Inst.* **2016**, *107*, 923–937. [CrossRef]
30. Deak, T.; Czigány, T. Chemical composition and mechanical properties of basalt and glass fibers: A comparison. *Text. Res. J.* **2009**, *79*, 645–651. [CrossRef]
31. *GB/T 50081-2019*; Standard for Test Methods of Concrete Physical and Mechanical Properties. National Standard of the People's Republic of China: Beijing, China, 2019.
32. *GB/T 228.1-2021*; Metallic Materials—Tensile Testing—Part 1: Method of Test at Room Temperature. National Standard of the People's Republic of China: Beijing, China, 2021.
33. *JGJ/T 101-2015*; Specification for Seismic Test of Buildings. National Standard of the People's Republic of China: Beijing, China, 2015.
34. Zhang, X.G.; Luo, C.Y.; Wang, J.B.; Kuang, X.M.; Huang, Y.J. The Axial Compression Behavior of Basalt Fiber-Reinforced Recycled Aggregate Concrete-Filled Circular Steel-Tubular Column. *Sustainability* **2023**, *15*, 14351. [CrossRef]
35. Nasrollahzadeh, K.; Nouhi, E. Fuzzy inference system to formulate compressive strength and ultimate strain of square concrete columns wrapped with fiber-reinforced polymer. *Neural Comput. Appl.* **2018**, *30*, 69–86. [CrossRef]
36. Han, L.H. *Concrete Filled Steel Tubular Structures—Theory and Practice*, 3rd ed.; Science Press: Beijing, China, 2016. (In Chinese)
37. Zhang, X.G.; Zhou, G.Q.; Fan, Y.H.; Gao, X.; Leng, F.G.; Wang, F. Axial compressive property of circular steel tubular stub column filled with basalt-fiber reinforced recycled-concrete. *Acta Mater. Compos. Sin.* **2023**, *40*, 369–382. (In Chinese)